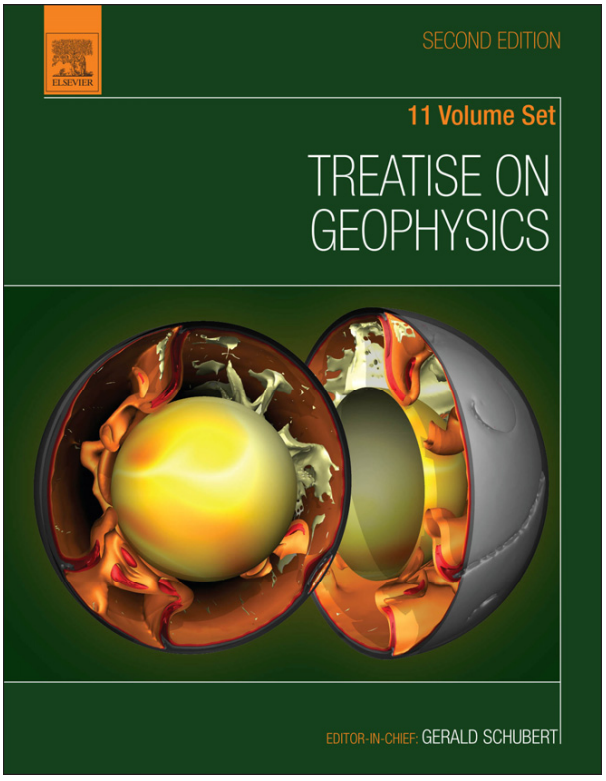

Dziewonski A.M., and Romanowicz B.A Deep Earth Seismology: An Introduction and Overview. In: Gerald Schubert (editor-in-chief) Treatise on Geophysics, 2nd edition, Vol 1. Oxford: Elsevier; 2015. p. 1-28.

1.01 Deep Earth Seismology: An Introduction and Overview

AM Dziewonski, Harvard University, Cambridge, MA, USA
BA Romanowicz, University of California, Berkeley, CA, USA; Collège de France, Paris, France

Applications of seismology to the study of the Earth's interior are only a little over 100 years old. Its tools in determining the properties of inaccessible Earth are the most powerful among all geophysical methods. The principal reasons are the availability of natural (earthquakes) or controlled (explosions and vibrators) sources of elastic waves and their relatively low attenuation with distance. Seismological methods span some six orders of magnitude in frequency, and the depth of an investigated structure may range from a few meters in engineering applications to the center of the Earth. Progress in seismology has been achieved through developments on several fronts: theory, instrumentation, and its deployment, as well as computational resources.

Even though the studies of earthquakes and the Earth's structure are closely related, the two subjects are often discussed separately. This volume is devoted to the Earth's structure and Volume 4 to studies of earthquakes. Nevertheless, the relationship is intimate. For example, it is possible to formulate an inverse problem in which earthquake locations are sought simultaneously with the parameters of the Earth's structure, including three-dimensional (3-D) models (see Chapter 1.10).

In the past 25 years, important progress has been made on several fronts: (1) the development of broadband digital instrumentation (see Chapter 1.02), which has allowed the construction of digital seismic databases of unprecedented quality at both the global and the regional scales; (2) the development of powerful data analysis tools, made possible by ever more efficient computer technology; and (3) theoretical progress in the forward and inverse computation of the effects of strong lateral heterogeneity on seismic-wave propagation. The combination of these factors has led to much improved images of structure at the global and regional scale, often helped by the inclusion of constraints from other types of data, primarily from the fields of mineral physics and geodynamics. This volume is thus divided into four parts. The first part principally covers seismic instrumentation, theoretical developments, and seismic data analysis techniques. Chapter 1.03 discusses the state of the art in the computation of the Earth's normal modes, while Chapter 1.04 describes progress in the measurements of normal-mode and long-period surface waves. Two chapters are devoted to the computation of synthetic seismograms in the presence of lateral heterogeneity, suitable for the case of body waves (see Chapters 1.05 and 1.06). Significant progress has recently been made in the computation of synthetic seismograms in a 3-D Earth using numerical methods. A review is given in Chapter 1.07. With the deployment of dense regional arrays of broadband seismometers, another area of rapid progress has been that of the adaptation of methodologies first developed in exploration seismology to the case of fine structure imaging of the crust and upper mantle at larger scale. These approaches are described in Chapter 1.08 for passive-source applications and in Chapter 1.15 for the case of active sources. The realization of the importance of anisotropy in the Earth has led to theoretical and methodological developments (see Chapters 1.09 and 1.18). Note that the issue of anisotropy is also discussed in Chapter 1.19 in the context of the inversion of surface-wave data. Inverse methods, in particular in the context of global and regional tomography, are discussed in Chapter 1.10.

In the second part of Volume 1, reviews of the status of our knowledge on the structure of the Earth's shallow layers are presented, starting with a global review of the Earth's crustal structure (see Chapter 1.11). During the last decade, there has been rapid development in using the Earth's noise as a source of the signal. A review of these developments is presented in Chapter 1.12. Two chapters discuss regional structure in the oceans: Chapter 1.13 for mid-ocean ridges and Chapter 1.14 for hot-spot swells. Chapter 1.18 presents results of studying anisotropy in subduction zones with particular attention devoted to the flow-induced preferential orientation of olivine crystals. Finally, two chapters are devoted to the results of regional experiments: upper-mantle studies using data from portable broadband experiments (see Chapter 1.16) and crustal studies, specifically in Europe, from high-resolution long-range active-source experiments (see Chapter 1.17).

The third part of this volume concerns the Earth's deep structure, divided into its main units: the upper mantle (see Chapter 1.19); the transition zone and upper-mantle discontinuities (see Chapter 1.21); regional tomography of

*Treatise on Geophysics, 2nd edition, (*2015), vol. 1, pp. 1-28

subducted slabs, with particular attention given their stagnation at the bottom of the transition zone (Chapter 1.20); the lower mantle; and the highly complex D″ region at the base of the mantle (Chapter 1.22) as well as the Earth's core (see Chapter 1.23). Chapter 1.24 is devoted to the subject of scattering in the Earth and Chapter 1.25 to that of attenuation. Finally, the fourth part of this volume comprises two chapters, in which constraints on the Earth's structure from fields other than seismology, mineral physics (see Chapter 1.26) and geodynamics (see Chapter 1.27), are discussed.

This volume addresses various aspects of 'structural seismology' and its applications to other fields of Earth sciences. Not all the subjects are covered in comparable detail, even though the completeness of the coverage was the initial objective of the editors. Compared to the 2007 edition of Volume 1 of *Treatise on Geophysics*, this edition contains four new (Chapters 1.02, 1.12, 1.18, and 1.20). Most of the other chapters have been significantly updated, except Chapters 1.14, 1.15, and 1.16, which are reprinted 'as is' from the 2007 edition.

In what follows, we briefly describe the developments in seismology from the end of the nineteenth century until the present, with the main emphasis on the development of instrumentation and its deployment, because seismology is a data-driven science. An account of the history of seismology can be found, among others, in Agnew et al. (2002). We also present our point of view, which some may consider controversial, specifically on current issues in global tomography and interpretation of the 3-D models not discussed in any of the chapters. We justify bringing these issues forward because of our belief that interpretation of tomographic results in terms of mantle dynamics does not match the robustness of models built using data that have good resolution at all depths in the mantle.

1.01.1 Developments from the Late Nineteenth Century until the Early 1950s

The theoretical beginnings of seismology may be traced to the eighteenth- and nineteenth-century studies of elasticity and propagation of elastic waves in solids. Lord Kelvin provided the first numerical estimate of the period of the fundamental vibrational mode ($_0S_2$) in 1863, but the development of the proper theory for a homogeneous sphere had to wait nearly 50 years (Love, 1911). Lord Rayleigh solved the problem of propagation of surface waves in an elastic half-space in 1877.

This preceded the first mechanical seismographs, which were developed in the 1880s. Originally, the seismographs had very low sensitivity and were used for the recording of local earthquakes. The history of global seismology begins with the recording of an earthquake in Japan on 19 April 1889 by von Rebeur-Paschwitz. He associated a disturbance recorded on a tiltmeter, used to study the Earth's tides, with the reports of a great earthquake in Japan. Figure 1 shows a copy of this recording as published in *Nature* (von Rebeur-Paschwitz, 1889, 1895).

The early seismographs were mechanical pendulums with no damping, other than friction. Their magnifications (the ratio of the amplitude on a seismogram to the actual ground motion) were very low, and because of the lack of damping, the records were very oscillatory and it was difficult to distinguish the arrivals of different phases. An improved mechanical

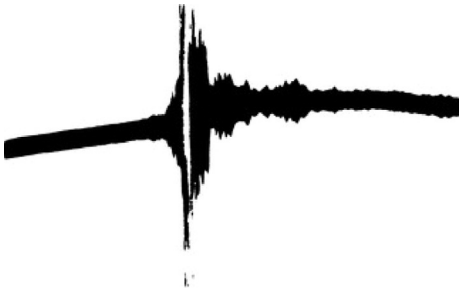

Figure 1 The historical first recording of a teleseismic event: an earthquake in Japan recorded in Potsdam on a tiltmeter designed by von Rebeur-Paschwitz. The early seismograms had difficulty with damping the pendulum motion and made phase identification difficult. Reproduced from von Rebeur-Paschwitz (1895) Horizontalpendal-Beobachtungen auf der Kaiserlichen Universitats-Sternwarte zu Strassburg 1892–1894. *Gerlands Beiträge zur Geophysik* 2: 211–536.

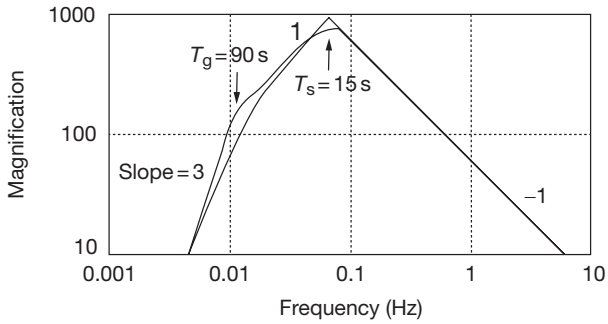

Figure 2 Plot of the ground-motion (amplitude) response of a World-Wide Standardized Seismograph Network (WWSSN) station with a seismograph free period (T_s) of 15 s and galvanometer with a free period (T_g) of 90 s. The segment between these two periods has a flat velocity response, characteristic of broadband seismometers. The response in modern instruments is shaped electronically; a typical FDSN station has a flat velocity response from 5 Hz to 360 s. Reproduced from Wielandt E (2002) Seismic sensors and their calibration. In: Bormann IP (ed.) *IASPEI New Manual of Seismological Observatory Practice*, vol. I, pp. 1–46. Potsdam: GeoForschungsZentrum Potsdam, Chapter 1.06.

seismograph with controlled damping was built by Wiechert in 1904. Soon afterward, Galitzin (1914) developed an electromagnetic seismograph system, where the motion of the seismometer's pendulum generated an electric current by motion of a coil in the magnetic field. This current was, in turn, carried to a galvanometer; the rotation of the galvanometer's coil in a magnetic field was recorded on photographic paper by a beam of light reflected from a mirror attached to the coil. The response of the system depended on the sensitivity and free period of the seismometer and of the galvanometer and their damping. While the system was more complex, it allowed for much more flexibility in selecting a desired response. Figure 2 shows the response of the seismograph–galvanometer system and gives an idea of the way it could be shaped by the choice of different free periods of the system's components. With gradual improvements, the seismometer–galvanometer system, recording on photographic paper, was commonly used during the following 60–70 years, when it was gradually replaced by digital systems (see Chapter 1.02).

With the improvement of the recording systems technology, phase identification became easier, and it was possible to identify P-arrivals (primary) corresponding to compressional waves, S-arrivals (secondary) corresponding to shear waves, and L-arrivals, sometimes called 'the main phase,' corresponding to surface waves. The surface waves caused some confusion because there was also a transverse motion, not predicted by Rayleigh. It was not until 1911 that Love showed that transversely polarized surface waves can propagate in a layered Earth.

Progress in the first decade of the twentieth century was rapid. Some classical problems such as computation and inversion of travel times for the velocity structure were solved by (Benndorf, 1905, 1906; Herglotz, 1907; Knott, 1899; Wiechert, 1907; Zöppritz, 1907) independently developed equations for the amplitude of reflected and transmitted waves at the boundary between two elastic media.

As regards the Earth's structure, there was a paper by Oldham (1906), in which he proposed the existence of the Earth's core, although there has been some confusion in identification of phases: what he thought to be a delayed S-wave was actually an SS (e.g., Schweitzer, 2007). Gutenberg (1913) properly identified reflections from the core–mantle boundary (CMB) and determined the radius of the core quite accurately, and Jeffreys (1926) showed that the core is liquid. Mohorovičić (1910) discovered the boundary between the crust and the upper mantle, thus beginning the era of studies of the crust and lithosphere, which greatly accelerated after World War II.

The first global seismographic networks (GSNs) were established in the early years of the twentieth century. The first one was deployed by John Milne in various countries of the British Commonwealth with the support of the British Association for the Advancement of Science and eventually consisted of 30 stations (Adams et al., 2002). The Jesuit Network was established soon afterward, with a particularly large number of instruments in the United States, but also including stations on all continents (Udias and Stauder, 2002). With a global coverage sufficient to locate large earthquakes, informal bulletins were published using the location method developed by Geiger (1910, 1912), which (with many modifications) is still used today. In 1922, the International Seismological Summary (ISS), with international governance, was established under Professor Turner of the University of Oxford with the charge to produce 'definitive global catalogs' from 1918 onward.

The slow progress in unraveling the Earth's structure culminated in the 1930s with the discovery of the inner core by Lehmann (1936) and the compressional velocity, shear velocity, and density models by Gutenberg (1913), Jeffreys (1926), and Bullen (1940). The Gutenberg and Jeffreys velocity models are shown in **Figure 3**; except for the details of the upper-mantle structure, these models are very similar to the modern ones. The low-velocity zone above the inner–outer core boundary in the model of Jeffreys illustrates the sometimes unfortunate tendency of seismologists to introduce physically implausible features in the model in order to match the data; Jeffreys needed to add a 2 s delay to match the inner-core travel times and accomplished it by inserting this feature, which is impossible to reconcile with the chemical and physical properties of materials in this depth range (Birch, 1952). The other important difference between the models of Jeffreys and Gutenberg was the existence of a low-velocity zone in the depth range 100–200 km in the upper mantle. There were very hot debates on this issue; it can now be explained by the fact that they used data from tectonically different regions; there is a pronounced low-velocity zone in the western United States, but not under the Eurasian shield regions.

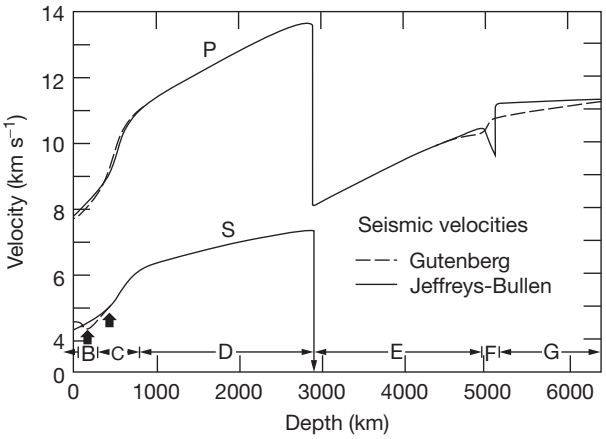

Figure 3 Comparison of the seismic velocity models of Gutenberg and Jeffreys, both built in the 1930s. The principal difference between the models is the presence of the low-velocity zone in the Gutenberg model and the structure near the inner–outer core boundary where the low-velocity zone in the Jeffreys model is erroneous and the velocity increase in the inner core is larger than in the Gutenberg model. With the exception of the transition zone (400–650 km depth), the modern models are not very different. Reproduced from Anderson DL (1963) Recent evidence concerning the structure and composition of the Earth's mantle. *Physics and Chemistry of the Earth* 6: 1–129.

With internal reflections and conversions of waves at the boundaries, seismologists developed a system of phase identification that reflects a combination of the types of waves (P or S), the region in which they propagate (K and I for the P-waves in the outer and inner core, respectively; PKIKP designates a phase that travels as P in the mantle, P in the outer core, and P in the inner core) and the boundary at which they were reflected (c for CMB and i for the inner–outer core boundary). A shear wave reflected once from the free surface at the midpoint of its path is designated by SS; higher multiple reflections, like SSS or SSSSS, can be observed by sampling a large volume of the Earth along their paths. For earthquakes with a finite focal depth, the P- and S-waves traveling upward from the source have designation of p or s; following reflection at the surface, they represent the so-called depth phases (e.g., pP and sP); the travel-time difference between the arrival of pP and P strongly depends on focal depth.

Figure 4 shows examples of various seismic phases, and **Figure 5** is the graphic representation of the travel times as a function of distance computed by Jeffreys and Bullen (1940) for the model of Jeffreys (1939). It is remarkable that this set of tables, including predictions for different focal depths, was calculated using a manual mechanical calculator! The data used by Jeffreys were extracted from the ISS, the precursor of the International Seismological Centre (ISC), which (with international financial support and governance) resumed the ISS role in 1964 and continues until today.

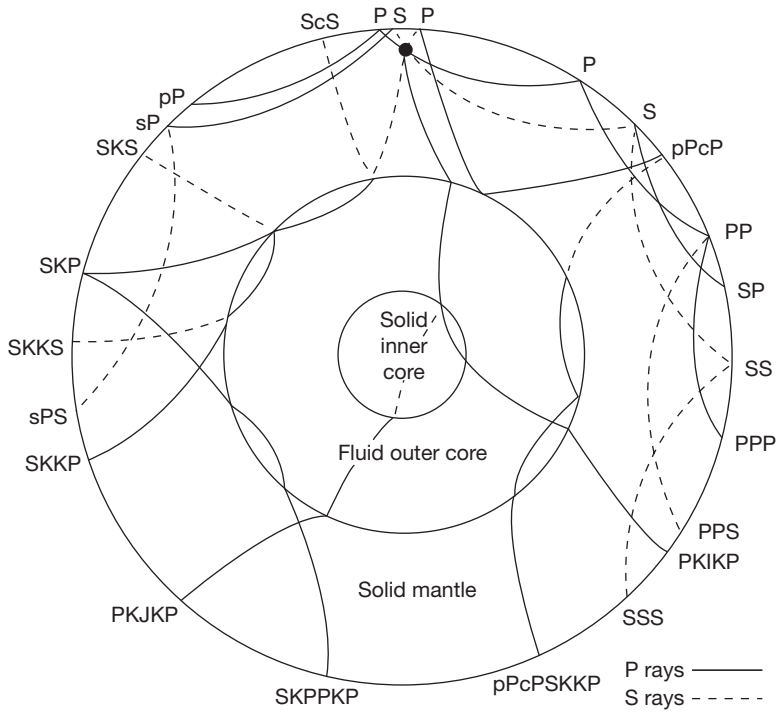

Figure 4 Examples of seismic rays and their nomenclature. The most commonly identified phases used in earthquake location are the first arriving phases: P and PKIKP. Reproduced from Stein S and Wysession M (2003) *An Introduction to Seismology, Earthquakes and Earth Structure*. Oxford: Blackwell, ISBN: 0865420785.

Bullen (1949) divided the Earth into a number of concentric shells, designated by letters from A to F; in this division, the lower mantle was designated by the letter D″. when Bullen recognized that the deepest 150 km of the lower mantle had an anomalously flat velocity gradient, he divided the region D into D′ and D″. More recently, and not entirely correctly, D″ came to signify the structure in the deepest 300 km, or so, of the lower mantle, which is characterized by a still-growing collection of structural and compositional complexities (see **Chapter 1.22**).

It was recognized relatively early that the dispersion of surface waves was different in the continents than in the oceans, with an indication that the oceanic crust was significantly thinner. Computing the dispersion of surface waves was algebraically and numerically difficult; the correct formulas for the dispersion of Rayleigh waves in a layer over a half-space were formulated by Stoneley (1928), and the case of the two layers over a half-space could be solved only for a very specific set of parameters.

1.01.2 Developments from 1950s to the Early 1980s

It must have been frustrating for seismologists not to be able to use information about the Earth's structure contained in the most prominent features of the seismograms: the dispersed surface waves. This changed when Haskell (1953) adapted to the case of elastic media the method first proposed by Thomson (1950) in the acoustics case. The approach made it possible to compute dispersion of surface waves (Rayleigh and Love) in a layered medium with an arbitrary number of layers over a half-space. It involved multiplication of matrices, one for each layer, changing the wave number for a fixed frequency such as to match the boundary conditions (vanishing of stresses) at the free surface. Because of the enormous amount of calculations to be performed, it required application of an electronic computer, and its application opened yet a new era in seismology. The Haskell's matrix method has been adapted to other problems in seismology, such as calculation of synthetic seismograms using the 'reflectivity method' (Fuchs and Müller, 1971). Electronic computers were at first very expensive and rare, and it was not until the 1960s that they became generally available at universities (Haskell worked at the Air Force Cambridge Research Laboratories).

Surface-wave dispersion began to be studied intensively in the 1950s principally at the Lamont Geological Observatory of Columbia University, primarily by Ewing and Press, who observed mantle waves in the 1952 Kamchatka earthquake, identifying arrivals from R6 to R15 (see **Chapter 1.04**) and measuring their group velocities up to a period of 500 s (Ewing and Press, 1954). Regional measurements of surface-wave dispersion were initiated by Press (1956). A monograph by Ewing et al. (1957) summarizes the state of the knowledge on seismic-wave propagation in layered media at that time. Ewing and Press also developed a true long-period seismograph, which was capable of recording mantle waves even for moderately sized earthquakes. This instrument was deployed at 10 globally distributed International Geophysical Year network stations operated by Lamont.

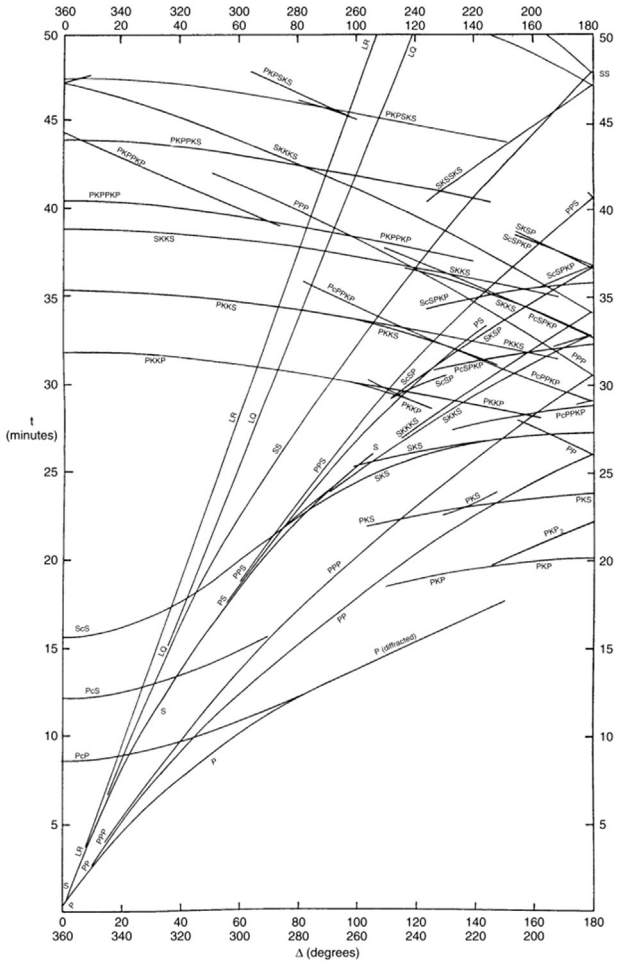

Figure 5 Travel times of seismic phases for the surface focus as computed by Jeffreys and Bullen (1940). Reproduced from Jeffreys H and Bullen KE (1940) *Seismological Tables*, p. 50. London: British Association for the Advancement of Science.

It is not often that a mistake leads to favorable results, but this was the case with the free oscillations of the Earth. Benioff (1958) reported an oscillation with a period of 57 min seen in the record of the 1952 Kamchatka earthquake. Even though this observation was eventually attributed to an artifact in the functioning of the instrument, it stimulated the theoretical and computational research needed to calculate eigenfrequencies for a realistic Earth model. Some of the calculations preceded Benioff's report (Jobert, 1956, 1957), but the efforts of Pekeris and Jarosch (1958) and Takeyuchi (1959) were clearly motivated to explain the observed period. These calculations, using the variational approach and the Jeffreys–Bullen Earth model, predicted the period of ${}_0S_2$ to be 52 min and that of ${}_0T_2$ 43.5 min. Neither was close enough to Benioff's 'observation.' The modern approach was developed by Alterman et al. (1959), who recast the system of three second-order partial differential equations into a system of six first-order differential equations, thus removing the need for differentiation of the elastic constants, and allowed the use of standard numerical methods to obtain the solution. Tests using the Gutenberg and the Jeffreys–Bullen models showed that they predict very similar free oscillation periods for the gravest modes but differ at shorter periods by 1–2%.

When the greatest instrumentally recorded earthquake of 20 May 1960 occurred in Chile, seismologists had all the tools (theory, computers, and instrumentation) needed to measure and interpret its recordings. Three back-to-back papers in a 1961 issue of the *Journal of Geophysical Research* reported the first correct measurements of free oscillation periods: Benioff et al., Ness et al. (1961), and Alsop et al. (1961). The observations were made on strainmeters in Isabella, Ñaña, and Ogdensburg; seismographs at Pasadena; and a gravimeter at the University of California, Los Angeles (UCLA). All three studies agreed in mode identification and found that their periods were very close to those predicted by the existing Earth models (Pekeris et al., 1961a). More detailed studies of the spectra revealed that they are split; the effect of the Earth's rotation was shown to explain this effect (Backus and Gilbert, 1961; Pekeris et al., 1961b). Thus, normal-mode seismology was born. Progress in the theory, particularly considering the effect of lateral heterogeneities and mode coupling, would extend over decades to come. First attempts at inversion of normal-mode data were not particularly successful; the density model of Landisman et al. (1965) was flat throughout the lower mantle, implying either a strong radial heterogeneity or an immensely superadiabatic temperature gradient.

Backus and Gilbert (1967), Backus and Gilbert (1968), and Backus and Gilbert (1970) provided the formal background for consideration of geophysical inverse problems, and even though their own experiments with inversion of normal-mode periods for the velocities and density, using a subset of normal-mode data, were discouraging (two very different models were found fitting the data nearly exactly; Backus and Gilbert, 1968), the idea of resolving kernels and trade-offs became part of the geophysical terminology.

Because seismic methods were considered essential in discriminating between earthquakes and nuclear explosions (Berkner et al., 1959), an intensive observational program, called Vela Uniform, was initiated. One of its components of great significance to studies of the Earth's interior was the World-Wide Standardized Seismograph Network (WWSSN), consisting of a set of three-component short-period and three-component long-period seismographs, with identical responses, except for magnification, which depended on local noise levels. At its peak, the WWSSN consisted of 125 stations (**Figure 6**), with distribution limited by geography and politics: there were no stations in the Soviet Union, China, and poorly developed areas in Africa and South America. The novel aspect of WWSSN was its standardized response and centralized system of distribution of copies of seismograms. Individual stations were sending the original seismograms to a central location, where they were microfilmed, using a very high-resolution camera, and then returned to the stations. A seismologist could request copies of seismograms for a particular date and receive them as either microfilm chips or photographic enlargements to the original size. Several larger institutions had a blanket order on all the records. This data accessibility represented major progress with respect to the earlier procedures, where one had to request copies of seismograms from individual stations, which greatly limited and delayed the research. WWSSN functioned for 20–25 years,

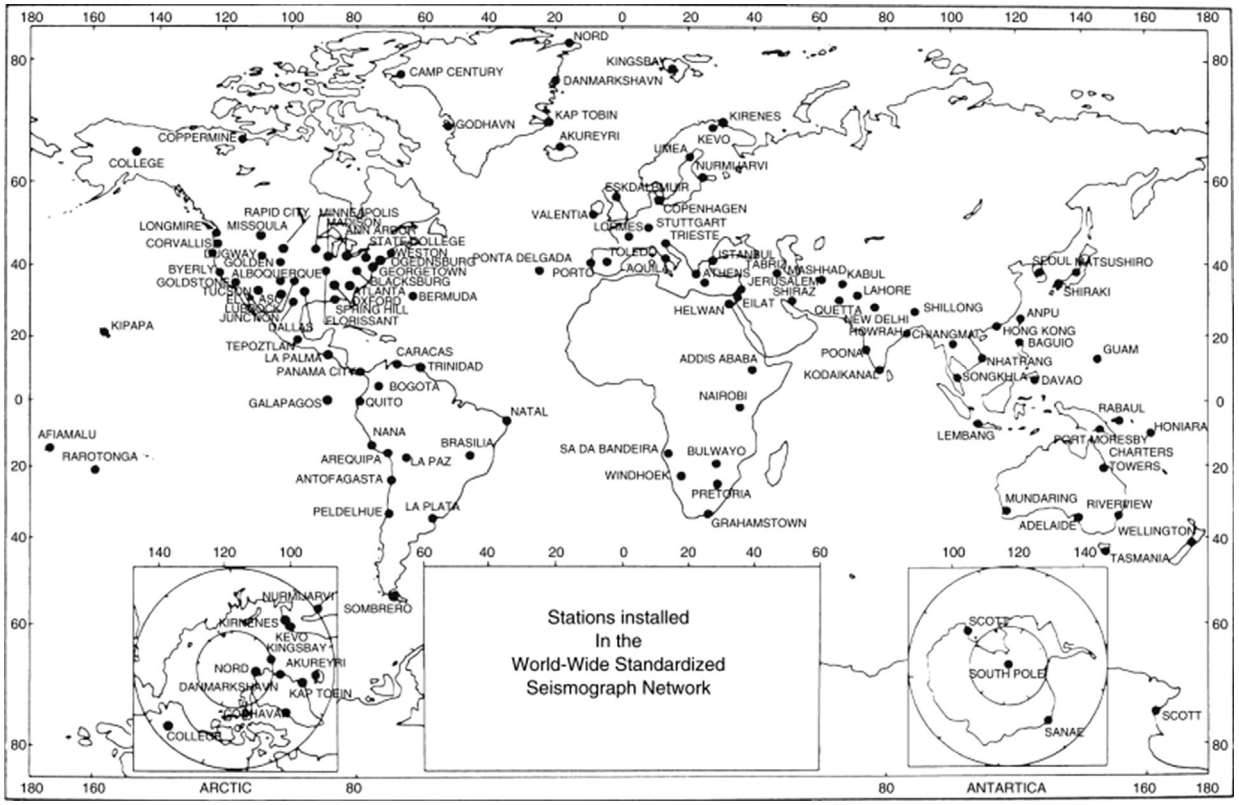

Figure 6 Map of the stations of WWSSN established in the early 1960s, following recommendations of Berkner et al. (1959). Courtesy of US Geological Survey.

slowly declining in the quality and number of stations; it ceased functioning in the late 1980s when data from new digital stations became available.

Another development of the 1960s was the introduction to seismology of digital recording, greatly facilitating research and the development of massive, computerized data-processing methods. One such facility, the large aperture seismic array (LASA), shown in Figure 7, was built in the mid-1960s in Montana. It consisted of six 'rings,' for a total of 21 subarrays, each with 25 short-period seismometers emplaced in boreholes, to improve the signal-to-noise ratio. The data were telemetered in real time to a central location in Billings, Montana, where they were processed for detection of a signal. Major scientific discoveries were made with this tool, particularly when weak signals were involved, for example, observations of reflections from the inner core. In practical terms, the array did not meet the expectations; the site response across this 200 km aperture array varied so much that the signals had limited coherency and signal enhancement by stacking was not as effective as expected. A somewhat smaller array was installed a few years later in Norway (NORSAR); elements of this array are still active and have been upgraded recently to modern, high-dynamic-range band–band response. Most of the arrays of the International Monitoring System (IMS) used for seismic discrimination purposes have an aperture of only several kilometers; because on that scale, the coherency at 1 Hz frequency can be achieved.

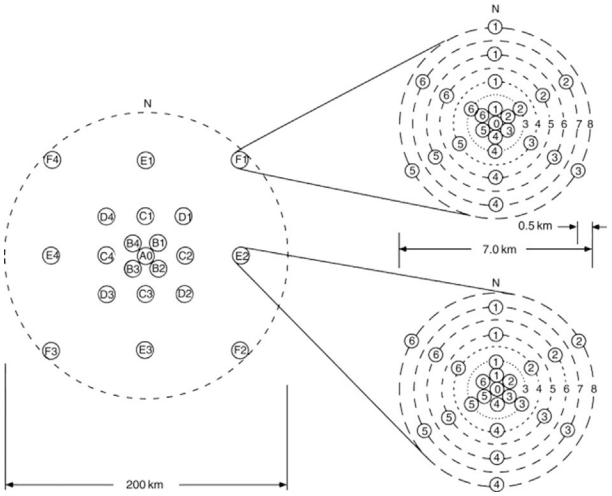

Figure 7 Configuration of the large aperture seismic array (LASA) and an expanded view of two of its subarrays. Reproduced from Stein S and Wysession M (2003) *An Introduction to Seismology, Earthquakes and Earth Structure*. Oxford: Blackwell, ISBN: 0865420785.

One of the important results obtained from the analysis of array data was the detection of upper-mantle discontinuities (Johnson, 1967), confirming the result predicted by experimental petrology that there should be two discontinuities at

pressures and temperatures corresponding to depths of about 400 and 650 km, respectively (Birch, 1952).

Surface-wave studies blossomed in the 1960s. At first, measurements of dispersion involved rather simple 'analog' methods, such as the peak-and-trough approach to measuring phase and group velocities. Some very important results were obtained in this way, such as the Canadian Shield study of Brune and Dorman (1963). Digital analysis, however, was soon to take over. Manual digitization of analogue recordings, WWSSN data in particular, became easier, and with increasing availability of computers and decreasing cost of computations, various techniques were developed, for the most part involving applications of the Fourier transform. With the development of the fast Fourier transform (FFT) algorithm (Cooley and Tukey, 1965), the cost of time-series analysis declined dramatically; a review by Dziewonski and Hales (1972) summarizes the state of the art at the beginning of the 1970s. Some of these methods, such as the multiple filtration technique to measure group velocity dispersion, residual dispersion measurements, and time-variable filtration, are still in use today. The 1960s have also seen the first studies of intrinsic attenuation by Anderson and Archambeau (1964), who developed partial derivatives (kernels) for Q from mantle-wave attenuation. Also, the first studies of lateral heterogeneity were conducted using the 'pure path' approach (Toksöz and Anderson, 1966).

Seismic experiments with controlled sources were conducted in a multi-institutional mode. One of the largest experiments was 'Early Rise' carried out in the July of 1966. A series of 38 explosions in Lake Superior of up to 5 tons of outdated torpedoes were used as the source of signals recorded by hundreds of seismometers – deployed by 12 governmental and academic groups – spreading radially in all directions. Signals were recorded as far as 2500 km, reaching teleseismic distances and providing a detailed profile of P velocity under a continental upper mantle (Green and Hales, 1968). A detailed review of crustal and upper-mantle studies with controlled sources is provided in **Chapter 1.11**.

With a large new data set, particularly measurements of previously unreported periods of long-period overtones provided by the analysis of free oscillations generated by the 1964 Alaskan earthquake and recorded at WWSSN stations (Dziewonski and Gilbert, 1972, 1973), studies of 1-D structure entered a new era. The resolution of this data set was sufficient to constrain the density profile in the mantle and the core; this turned out to be quite consistent with the behavior, in the lower mantle and outer core, of a homogeneous material under adiabatic compression. Jordan and Anderson (1974) were the first to combine the normal-mode and travel-time data, including differential travel-time data.

Numerous additional overtone data were obtained by Mendiguren (1973) and Gilbert and Dziewonski (1975) by introducing phase equalization techniques, such as 'stacking' and 'stripping.' These methods require the knowledge of the source mechanism to predict the proper phase for each seismogram to be considered; this in itself turned out to be a challenging inverse problem. Dziewonski and Gilbert (1974) derived the spectrum of all six components of the moment-rate tensor as a function of time for two deep earthquakes (Brazil, 1963; Colombia, 1970). For both events, they detected a precursive isotropic component. Eventually, this turned out to be an artifact of coupling between toroidal and spheroidal (Russakoff et al., 1998) modes, but the requisite theory to consider this effect was not available until 1984. Gilbert and Dziewonski (1975) presented two models based on measurements of eigenfrequencies of 1064 modes and mass and moment of inertia for a total of 1066 data. They derived two models 1066A and 1066B, with the first being smooth through the transition zone and the latter including the 400 and 660 km discontinuities; both models fit the data equally well.

At the 1971 General Assembly of the International Union of Geodesy and Geophysics (IUGG) in Moscow, the need for a reference Earth model was stated, and a Standard Earth Model Committee formed under the chairmanship of Keith Bullen. The Committee appointed several subcommittees, including one for the radius of the CMB: there were discrepancies on the order of 10 km at the time. The value recommended by the subcommittee was 3484 km (Dziewonski and Haddon, 1974), which – within 1 km – withstood the trial of time. Hales et al. (1974) proposed that the seismic velocities and density in the standard Earth model should be described by a low-order polynomial, with discontinuities at the appropriate depths. Dziewonski et al. (1975) constructed such a model, named parametric Earth model (PEM), which satisfied the normal-mode, travel-time, and surface-wave data. The novelty of this model was that, in a single inversion, different structures were obtained for the continental and oceanic crust and upper mantle. The normal-mode periods predicted by these two models (PEM-O and PEM-C) averaged in 2/3 and 1/3 proportion were constrained to match the observed periods and teleseismic travel times but separate data sets for continental and oceanic surface-wave dispersion. The differences between these two models ceased at the 400 km discontinuity, at which depth they became identical with the average Earth model, PEM-A.

The drawback of the PEM and all the previous models was that they did not consider the physical dispersion due to anelastic attenuation. For a signal propagating in an attenuating medium to be causal, the wave with higher frequencies must propagate with higher velocities. Thus, waves with a frequency of 1 Hz will propagate more rapidly than waves at a frequency of 1 mHz. In order to reconcile the seismic data that span 3.5 orders of magnitude, it is necessary to consider the frequency dependence of elastic parameters. This was pointed out by Liu et al. (1976). The Preliminary Reference Earth Model (PREM) constructed by Dziewonski and Anderson (1981), following the idea of parametric representation, considered the frequency dependence using the assumption that Q is constant in the band from 0.3 mHz to 1 Hz.

This necessitated obtaining the radial profiles of Q_μ and Q_κ; fortunately, there were new measurements available of normal-mode and surface-wave Q (Sailor and Dziewonski, 1978) such that a formal inversion for Q could be conducted simultaneously with the inversion for the velocities and density. It was recognized earlier that to explain the observed attenuation of radial modes, which contain a very high percentage of compressional energy (97.5% for ${}_0S_0$), it was necessary to introduce a finite bulk attenuation; Anderson and Hart (1978) preferred to place it in the inner core, and Sailor and

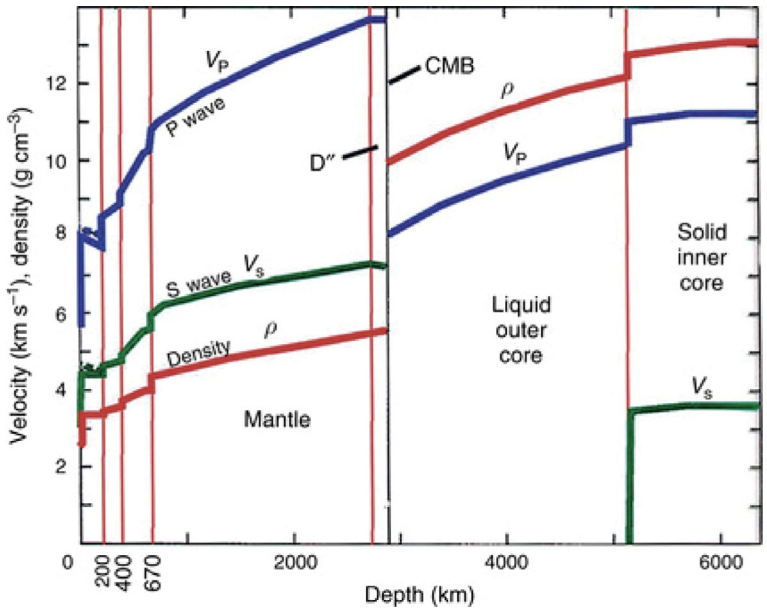

Figure 8 The Preliminary Reference Earth Model (PREM) of Dziewonski and Anderson (1981). In addition to the distribution of seismic velocities and density, PREM contains also the distribution of attenuation of the shear and compressional energy. From the website of Ed Garnero.

Dziewonski (1978) thought that Q_κ is finite in the upper mantle; unfortunately, the radial modes do not have the requisite depth resolution. Figure 8 shows the seismic velocities and density as a function of radius; the attenuation in PREM is discussed in Chapter 1.25. Another novel aspect of PREM was its radial anisotropy between the Moho and 220 km depth. This feature, at first suspected to be an artifact of the nonlinearity of the inverse problem, has been confirmed by global tomographic studies (e.g., Ekström and Dziewonski, 1998). The PREM model remains to this day a widely used 1D reference model for seismological studies based on long period data. For P wave studies, especially those concerning core sensitive phases, model AK135 (Kennett et al., 1995), which was built to constrain a global dataset of travel times from the ISC bulletins, is often preferred as a 1D reference model. It is to be noted, however, that this model includes a 36 km continental crust, and cannot be used for waveform modeling outside of continental areas.

The 1970s have also seen the beginning of seismic tomography; two studies published simultaneously (Aki et al., 1977; Dziewonski et al., 1977) addressed the problem on different scales: regional and global. Aki et al. solved for 3-D velocity structure under the NORSAR array, while Dziewonski et al. obtained a very low-resolution model of 3-D velocity perturbations in the entire mantle and showed significant correlation between velocity anomalies in the lowermost mantle and the gravest harmonics of the gravity field. The study of Dziewonski et al. (1977) was motivated by a paper by Julian and Sengupta (1973) who noticed that travel times for rays bottoming in the same region of the mantle tend to show similar residuals. They interpreted this result qualitatively as the evidence of lateral velocity variations; no modeling was presented in that paper. The first continental-scale 3-D model of the upper mantle, under North America, was published by Romanowicz (1979).

Two digital seismographic networks were established in the mid-1970s. One was the International Deployment of Accelerometers (IDA; Agnew et al., 1976, 1986), consisting of 18 globally distributed LaCoste–Romberg gravimeters with a feedback system that allowed digitization of the signal. It was designed to record very long-period waves, including the gravest modes of free oscillations of the Earth: one sample was taken every 20 s (later changed to 10 s). Only the vertical component of acceleration was recorded and the word length was 12 bits; the dynamic range was, therefore, rather limited but still considerably greater than that of analogue recordings. The sensitivity was set such that the scale was saturated for the first surface-wave arrivals for events with magnitude 7.0, or so, depending on the station's distance from the source and radiation pattern. The IDA network was operated by the Scripps Institution of Oceanography, and the centrally collected data were freely distributed to the academic community. This later became the future standard in global seismology. An early illustration of the power of such a global array was the analysis of the splitting of the gravest modes of free oscillations generated by the 1977 Sumbawa earthquake (Buland et al., 1979; M_w only 8.4).

The other network consisted originally of nine installations called Seismic Research Observatories (SROs) and five Abbreviated Seismic Research Observatories (ASROs). The SROs used borehole instruments, with significantly suppressed wind-generated noise levels, particularly on horizontal components. The ASROs were placed in underground tunnels or mine shafts and the seismographs were protected from the effects of changing pressure and temperature. The instrumentation is described by Peterson et al. (1976). This network was designed for monitoring the Nuclear Test Ban Treaty and high sensitivity was the main objective. In order to increase the dynamic range, the signal was sharply band-pass-filtered, so that at very long periods (>200 s), the response to acceleration was falling as ω^{-3}, while it was flat for the IDA instruments.

Even so, the SRO and ASRO stations were able to produce useful mantle-wave records for events with magnitude greater than about 6.5. Later, the network was augmented by 10 WWSSN stations, with the analogue output amplified and digitized at 16-bit analog to digital converters. The entire system was called Global Digital Seismographic Network (GDSN). There was no general data distribution system, but data for selected dates were available upon request from the Albuquerque Seismological Laboratory.

Until then, a seismic station typically comprised a set of seismometers with either 'long-period' or 'short-period' responses, or sometimes, as was the case for the WWSSN, one of each. This setup was designed at the time of analogue recording to avoid the microseismic noise peak around 6–7 s period, which would have made it impossible to digitize all but the largest earthquake signals. With digital recording, and the possibility of filtering out the microseismic noise by post-processing, this traditional instrument design became unnecessary.

A very important development in seismic instrumentation took place in Germany in the mid-1970s. An array of a new kind of instruments with digital recording was deployed near Gräfenberg (Harjes and Seidl, 1978). It used a novel feedback seismograph (Wielandt and Streckeisen, 1982). The system was rapidly recognized for its linearity and large dynamic range within a wide band of frequencies – hence the name 'broadband.' The Gräfenberg array's central station had been colocated with the SRO borehole station GRFO, and the comparisons were very favorable for the broadband instruments, which were capable of reproducing different narrowband responses using a single data stream. This type of instrumentation became the pattern for future developments (e.g., **Chapter 1.02**).

In addition to the developments in instrumentation, the late 1970s saw important theoretical developments, related to the asymptotic properties and coupling of the normal modes. Examples of such developments are papers by Woodhouse and Dahlen (1978), Jordan (1978), and Woodhouse and Girnius (1982).

1.01.3 From 1980 to Present: The Era of Tomography and Broadband Digital Seismic Networks

The data from both global networks of the 1970s led to results that demonstrated the need for development of a global network that would better satisfy the needs of basic research in seismology; three studies are noteworthy. A robust method, which uses entire segments of (digital) seismograms, was developed to obtain reliable mechanisms of earthquakes with magnitude 5.0 and above (Dziewonski et al., 1981; Ekström et al., 2005). In addition, the method refines the location of the source, which for an event of finite size need not be identical with the hypocenter determined from the first arrivals of the P-waves. This topic is discussed at length in **Chapter 4.16**. The reason why the subject is brought up here is that in most aspects of using waveform analysis for the purpose of drawing inferences about the Earth's structure, it is necessary to know the source mechanism. The so-called 'centroid moment tensor' method has now been applied to over 40 000 earthquakes from 1976 till present, and this catalog is available online (http://www.globalcmt.org).

Masters et al. (1982) measured center frequencies of spectral peaks of the fundamental spheroidal mode from hundreds of IDA records and discovered that there are spatially distinct patterns in the frequency shifts when plotted at locations of the poles of the great circles corresponding to the paths between the source and the receiver. By fitting spherical harmonics (even degrees only, because of the symmetry), these authors realized that the pattern is dominated by spherical harmonics of degree 2, an observation also made from great-circling surface waves by Souriau and Souriau (1983). **Figure 9** shows the pattern of the shifts of spectral peaks and zero line of the best-fitting spherical harmonics of degree 2 for four groups of ${}_0S_\ell$ modes with different ranges of degree ℓ. Note that the modes with the lowest ℓ show a different pattern than the remaining three groups. Our current understanding of this fact is that the low-ℓ modes sample deeper structure (lower mantle) than the higher-ℓ groups that predominantly sample the upper mantle. The authors performed a parameter search, in which they changed the radii of a shell in which the anomaly is located. The best variance reduction was for the anomaly placed in the transition zone. The lasting importance of this chapter is that it demonstrated that heterogeneity of very large wavelength and sizeable amplitude ($\pm 1.5\%$) exists in the Earth's interior.

Following the development of a waveform-fitting technique that allowed the simultaneous measurement of phase velocity and attenuation along a great-circle path (Dziewonski and Steim, 1982), Woodhouse and Dziewonski (1984) developed an approach to the interpretation of waveforms that could extract both the even and the odd harmonic coefficients of lateral heterogeneity as a function of depth. This method involves the 'path average approximation,' sometimes called PAVA. The seismograms are represented as a sum of all normal modes (spheroidal and toroidal) up to a certain frequency ω_{max}. For a given great circle, each mode is assumed to be affected by the average deviation from reference structure along the great-circle path (which is sensitive only to even-order harmonics) and along the minor-circle path (sensitive to both even and odd harmonics). The effect of the great-circle path can be modeled by a shift in eigenfrequency of the mode; the effect of the minor-arc structure is modeled by a fictitious shift of the epicentral distance for that mode; this shift depends on both even and odd parts of the structure. Woodhouse and Dziewonski (1984) processed about 2000 mantle-wave seismograms from the GDSN and IDA networks and obtained a model of the upper mantle (Moho – 670 km), M84C, using as basis functions spherical harmonics up to degree 8 for horizontal variations and Legendre polynomials as a function of radius up to degree 3. **Figure 10** shows a map of shear velocity anomalies at a depth of 100 km; there was no a priori information used on the location of the plate boundaries. Corrections were made for crustal thickness, recognizing only the continental and oceanic structure. An experimental model, M84A, obtained without applying crustal corrections, showed that not taking crustal thickness into account may result in mapping artificial anomalies at depths as large as 300 km. Model M84C had a strong degree-2 anomaly in the transition zone, confirming the results of Masters et al. (1982).

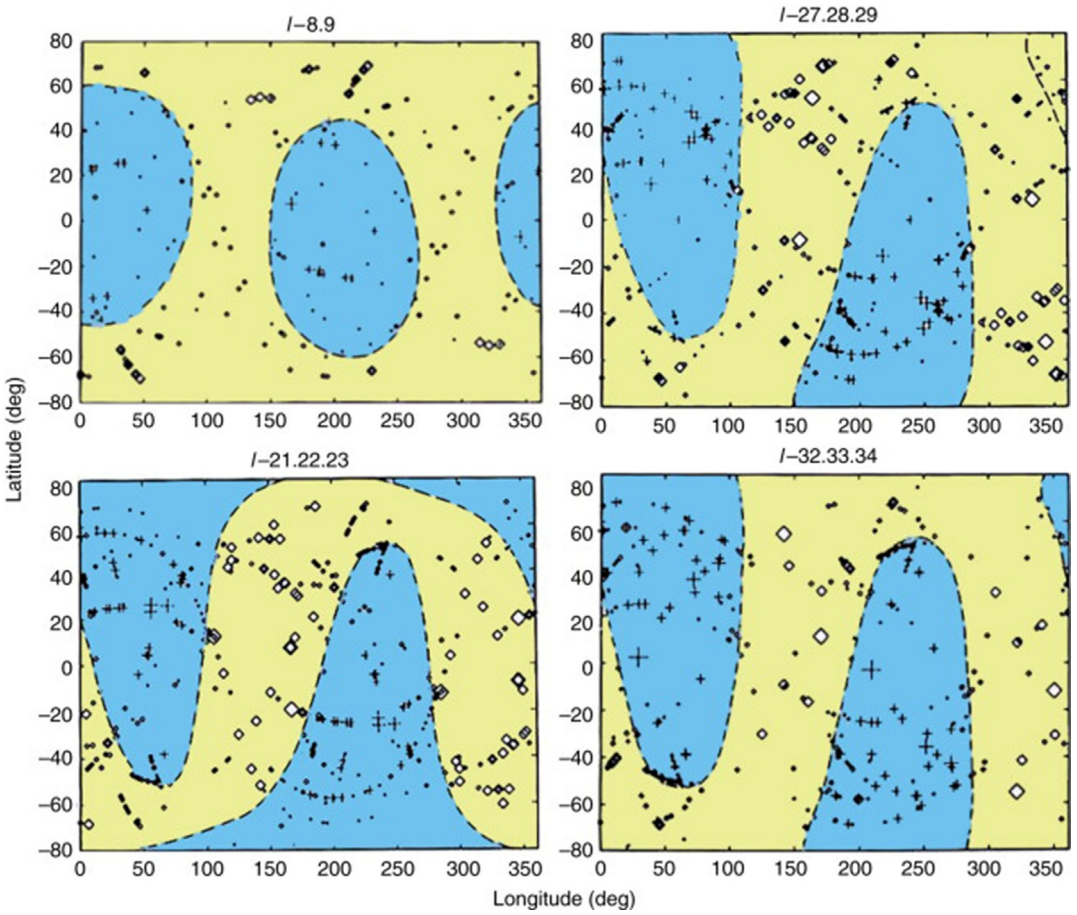

Figure 9 Maps of the observed frequency shifts of the fundamental spheroidal modes for four ranges of the order numbers as reported by Masters et al. (1982). The frequency shifts are plotted at the poles of the individual great-circle paths. It indicates the presence of very large wavelength–velocity anomalies in the Earth's interior; the preferred location of the source of the anomaly shown in the figure is the transition zone. However, the frequency shifts for the largest wavelength panel (top left; modes ${}_0S_8$ and ${}_0S_9$) show a different pattern than in the other three panels (modes from ${}_0S_{27}$ to ${}_0S_{34}$); the low-ℓ data have the greatest sensitivity in the lower mantle. Modified from Masters G, Jordan TH, Silver PG, and Gilbert F (1982) Aspherical Earth structure from fundamental spheroidal mode data. *Nature* 298: 609–613.

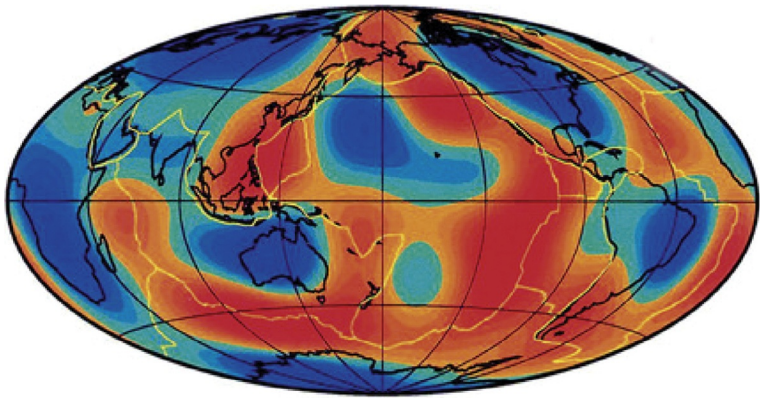

Figure 10 Shear velocity anomalies at a depth of 100 km in the model M84C of Woodhouse and Dziewonski (1984). The scale range is $\pm$5% and the resolving half-wavelength is 2500 km. Plate boundaries are shown as thin yellow lines. Except for the correction for crustal thickness, there was no other a priori information included in the inversion. Thus, the result demonstrates that the waveform inversion approach is able to distinguish the slow velocities under the mid-ocean ridges and ancient cratons, for example.

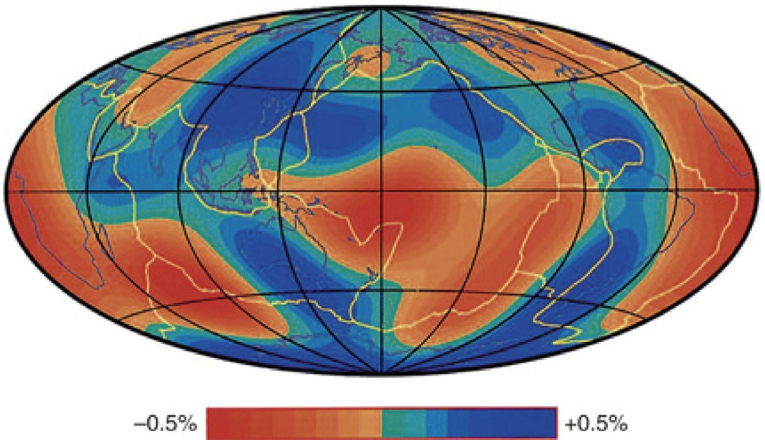

Figure 11 Map of P-velocity anomalies at a depth of 2500 km in model of Dziewonski (1984) derived from inversion of travel-time anomalies from ISC Bulletins. The resolving half-wavelength of the model is about 3500 km (at the surface). The model, dominated by the harmonics 2 and 3, clearly shows two large superplumes (African and Pacific) and the ring of fast velocities circumscribing the Pacific Rim. The scale is ±0.5%.

Another result also affected future developments, even though this study was not based on waveform analysis, but on the ISC bulletin data. With greater computational resources, it was possible to cast the inverse problem for lateral heterogeneities in the lower mantle on a larger scale using a substantially greater body of data than in Dziewonski et al. (1977). Unlike in this earlier study, in which blocks were used, Dziewonski (1984) used global basis functions: spherical harmonics representing horizontal variations and Legendre polynomials for radial variations. The degree of expansion was modest: only degree 6 in harmonics and degree 4 in radius, with the inversion limited to lower-mantle structure. In many ways, this new study confirmed the earlier one – including the correlation of lower-mantle structure with the gravity field (Dziewonski et al., 1977) – but it showed resolution of a truly remarkable concentration of the power of heterogeneity in low-order harmonics. Figure 11 shows a map of P-velocity anomalies at a depth of 2500 km. The structure, dominated by degree 2 (and, to a lesser extent, degree 3), shows two large slow regions, which came to be known as the African and Pacific 'superplumes', and a ring of fast velocities around the Pacific.

Why does global tomography work? Some suspected that truncation of the expansion at relatively low harmonic order may lead to aliasing and structures dominated by degrees 2 and 3, such as the one shown in Figure 11, are an artifact. The short answer is that global mantle heterogeneity has a 'red' spectrum. That is, the power spectrum of the spherical harmonic expansion begins to drop rapidly above a certain wave number ('corner wave number'). Su and Dziewonski (1991, 1992) showed that it is clearly visible even in data, such as maps of travel-time anomalies of SS-S or ScS-S. The concept is illustrated in Figure 12, using the continent–ocean variations of crustal thickness.

Figure 12 illustrates the point that for functions with a 'red' spectrum that is flat for small wave numbers but rapidly decreasing for larger wave numbers, it is possible to extract most of the signal using the 'red' part of the spectrum. Panel (a) shows the power spectrum of the continent–ocean function. It is flat for degrees from 1 to 5, and then, the power is offset at degree 6 and begins to decrease rapidly, roughly as ℓ^{-2}; the 'corner wave number' is in this case $\ell = 5$. Part (b) is the synthesis of this function using degrees from 1 to 8 (81 coefficients). The shapes of the continents are clearly recognizable, but details of the coastlines or islands are missing. Panel (c) shows the result of a synthesis using harmonics from 1 to 32 (1089 coefficients or 15 times more). There is an obvious improvement: Madagascar, New Zealand, Japanese Islands, Gulf of Mexico, can be identified, but the principal information on the outline of continental masses is already contained in panel (b).

Another point is that power at degree 32 is two orders of magnitude less than at degree 3. Actually, it is lower by three orders for the individual $Y_{\ell m}$ coefficients, since we define the power as the sum of all squared coefficients of degree ℓ. It is impractical to think that such a large range of values could be resolved in an inverse problem, particularly because the strength of the kernels commonly decreases with increasing wave number (see Figure 3 a–d in Dziewonski, 1984). However, if the continents were broken up into many smaller 'islands,' then a synthesis of the spherical harmonic coefficients up to degree 8 might be misleading and provide an aliased picture.

The 'corner wave number' seems to be a feature of many geophysically important functions: Su and Dziewonski (1992) showed that it occurs in spectra of several global functions, such as free air gravity, SS-S travel-time residuals, phase velocity, and 3-D models, which have a power spectrum that is relatively flat up to degrees from 6 to 8, after which it begins to decrease as ℓ^{-2}. This seems typical of the spectra of two-dimensional functions that are characterized by a set of large 'patches,' such as the large land masses in the continent–ocean function. If the spherical harmonic expansion is truncated at an order number beyond the corner wave number, the synthesis of such truncated series retains the main character of the original function (e.g., Figure 12). Similarly, an inversion for a truncated series of spherical harmonic coefficients does not introduce aliasing if truncation occurs in the steeply decreasing part of the power spectrum. Of course, there are some geophysically important functions

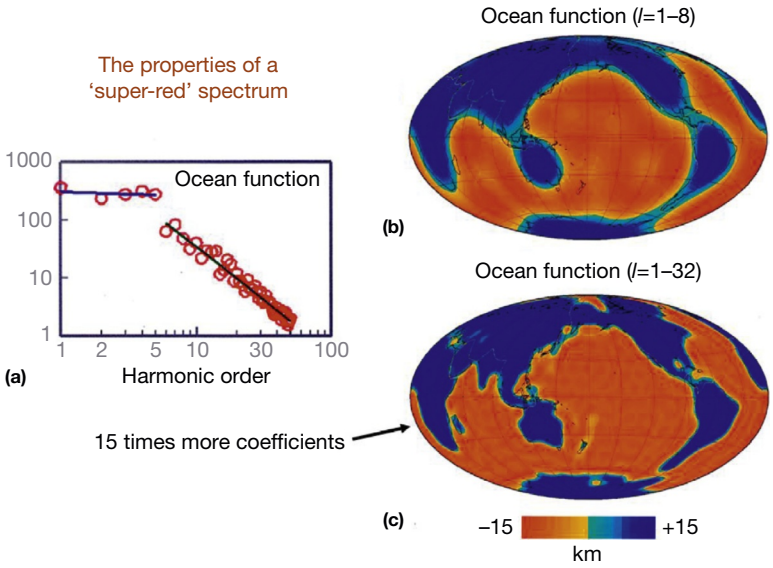

Figure 12 An example of a global function with a 'super red' spectrum. Crustal thickness under the oceans and continents, with a constant crust thickness for a given type, is expanded in spherical harmonics and then synthesized using a different cutoff wave number. Panel (a) shows the power spectrum of the continent–ocean function. Note the nearly flat spectrum for orders from 1 to 5 and then nearly linear decrease (in the log–log scale) for orders 6 and higher. The slope of that line is about ℓ^{-2}; the corner wave number is $\ell = 5$ in this case. Panel (b) shows the synthesized continent–ocean function for $\ell_{max} = 8$. All contours of continents are delineated and much of the variance is explained by this low-order model; this expansion has been used by Woodhouse and Dziewonski (1984) to introduce corrections for crustal structure. Panel (c) shows the result of a synthesis using $\ell_{max} = 32$. The details such as coastline and recovery of larger islands are clear, but they are achieved by using about 15 times more coefficients than those used to obtain panel (b). Also, the coefficients at higher wave numbers are very small, and it would be unlikely to be correctly derived through an inversion of observations with errors.

whose spectra have distinctly different characters, for example, linear features (slabs) have power spectra that are flat with harmonic order; point-like features (plumes?) have power spectra whose values increase with ℓ. In these cases, truncation would result in significantly lower amplitudes in the low-pass-filtered image.

This could also happen if the truncation of the spectrum occurred before the corner wave number. An example of the consequences of such an action is given by Mégnin et al. (1997). In a synthetic test, they limited to degree-6 inversion of waveform data calculated for a degree-12 model and showed that the results are aliased by the missing part of the structure (degrees 7 through 12). But in their test, the power spectrum had a maximum at degrees 6 and 7, and truncation at the maximum power is bound to cause aliasing. Boschi and Dziewonski (1999) demonstrated that there is no aliasing when travel times computed for a degree 40 model are inverted for a synthetic model limited to degree 12 (their plate 6), but the truncation was applied at the corner wave number.

Thus, in the 1980s, seismologists demonstrated that they can resolve 3-D structure within the Earth interior, giving the promise of an unprecedented ability to look at a present-day snapshot of mantle dynamics. Yet, the observing networks were in decline, with the support for the GDSN likely to be discontinued altogether and the original IDA network (limited to recording of vertical-component mantle waves and free oscillations) not meeting the needs of the broader community. In 1983, a plan was put forward to create a GSN of some 100 broadband, three-component seismographic stations sending the data in nearly real time to a central collection facility. The expectation was that this network would be supported by the National Science Foundation (NSF), in analogy to NSF supporting astronomy facilities. At the same time, seismologists using portable instrumentation came to the realization that they needed a centralized and standardized instrument pool. This led to the formation of a project called Portable Array for Seismic Studies of the Continental Lithosphere – PASSCAL. The GSN and PASSCAL groups merged and formed a consortium known as Incorporated Research Institutions for Seismology (IRIS), which incorporated in 1984.

At the same time, Steim (1986) was developing at Harvard his very broadband (VBB) instrument, based on the STS-1 broadband seismograph (Wielandt and Steim, 1986), and a very high-resolution (24-bit) digitizer. The response of a VBB instrument is designed to have a flat response to ground velocity between 5 Hz and 3 mHz, that is, over more than three orders of magnitude. Such an instrument had to have a very large dynamic range, of about 140 dB to span the range of ground velocities from the minimum Earth noise to a magnitude 9.4 earthquake at 30° epicentral distance. All these requirements were met, and Steim's VBB system became the design goal for the GSN and other networks. **Figure 13** shows the operating range of the system, and **Figure 14** illustrates the dynamic range of the GSN station in Albuquerque. The high-pass-filtered (75 s) record of the Sumatra–Andaman $M_w = 9.3$ earthquake shows surface waves with an amplitude of several millimeters and a record of a local microearthquake ($M < 1$) extracted from the same record; the ratio of the amplitudes is about 10 000 000! **Chapter 1.02** describes in detail the concept and history of the modern broadband

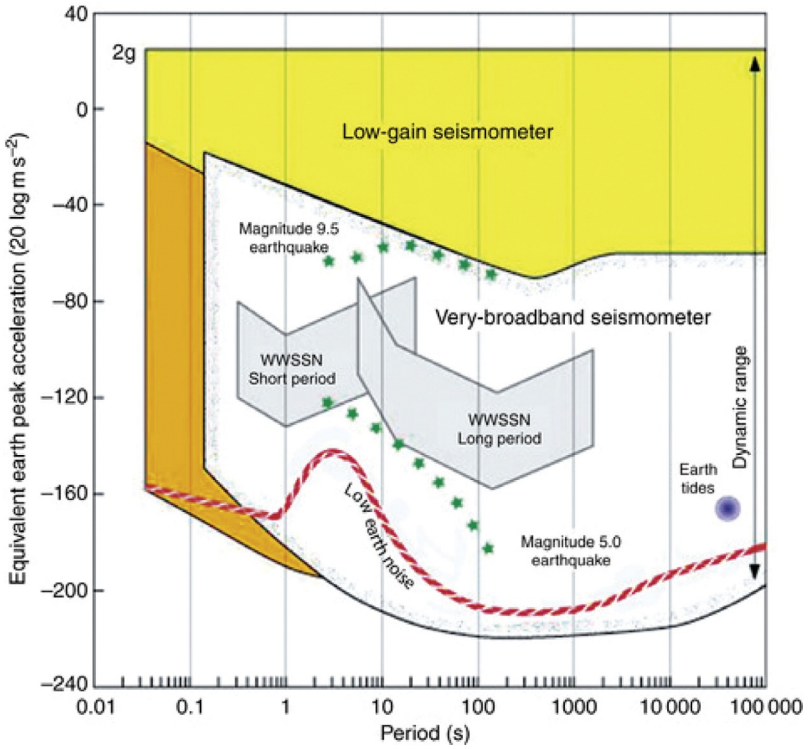

Figure 13 The dynamic range of the VBB channels of a Global Seismographic Network station. The range of the WWSSN short- and long-period channels are shown for comparison. At some GSN stations, the VBB channels are augmented by very short-period channels and accelerometers. The response was designed to resolve the ground noise from 5 Hz to tidal frequencies and to record on scale a magnitude 9 earthquake at a distance of 30°. Courtesy of IRIS.

digital seismograph that has now been implemented in stations of the global international network as well as many regional seismic networks.

Meanwhile, as the US seismologists were organizing themselves, a French effort named GEOSCOPE had already began taking shape. The objective of GEOSCOPE was the establishment of a global network of some 20–25 broadband digital seismographic stations utilizing the STS-1 seismometer, and destined in priority for locations around the world that filled gaps in the distribution of seismic stations. The project had officially begun in 1982, and in 1984, there were already five operational stations (Romanowicz et al., 1984), and 13 in 1986, (e.g., Romanowicz et al., 1991; Roult et al., 2010a,b).

While telemetry of the data was established later (in 1987), the state of health of the remote stations was monitored from early on using the satellite system Argos, which greatly facilitated their maintenance. As it was clear that it was inefficient to have two competing global networks, the need for a framework for international cooperation arose. Also, many countries were interested in deploying broadband instrumentation for their national or regional purposes and were agreeable to share these data. The international Federation of Digital Seismographic Networks (FDSN) was formed in 1986 (Romanowicz and Dziewonski, 1986), with the purpose of coordinating site selection, data exchange, and standardizing instrument responses. The FDSN has been very successful in achieving these goals, despite the fact that it is a purely voluntary, zero-budget organization. Figure 15 shows a map of the FDSN network as of January 2014 (after some 25 years of development); there are over 200 participating VBB stations, most of which now send data in nearly real time.

Similarly impressive progress was made in the area of field seismology, where progress in electronics led to overall improvement of the portability of the equipment and, in particular, reduction of power requirements, which makes operations much easier. In parallel with the development of the PASSCAL program of IRIS in the United States (see Chapter 1.16), other portable arrays were developed in other countries in the last 20 years, such as the LITHOPROBE cross continental project in Canada (Hammer et al., 2010), Lithoscope program in France (Poupinet et al., 1989), or the SKIPPY array in Australia (van der Hilst et al., 1994). Most recently, an ambitious program, USArray, was launched in the United States in 2007 as part of the EarthScope project. USArray is aimed at a systematic investigation of the structure under the contiguous United States with uniform resolution. It consists of three parts: a Permanent Array of 100 stations (the 'backbone' or 'reference array'), a Transportable Array (TA), and a Flexible Array (FA). The FA provides some 300 broadband seismographs and over 1000 active-source instruments, for experiments proposed by individual research groups, aimed at elaborating detailed local structure. The TA is the largest component of the program, and it consists of 400 broadband seismograph systems that, starting from the West Coast of the United States, have been moving gradually across the continental United States to cover the entire area with, roughly,

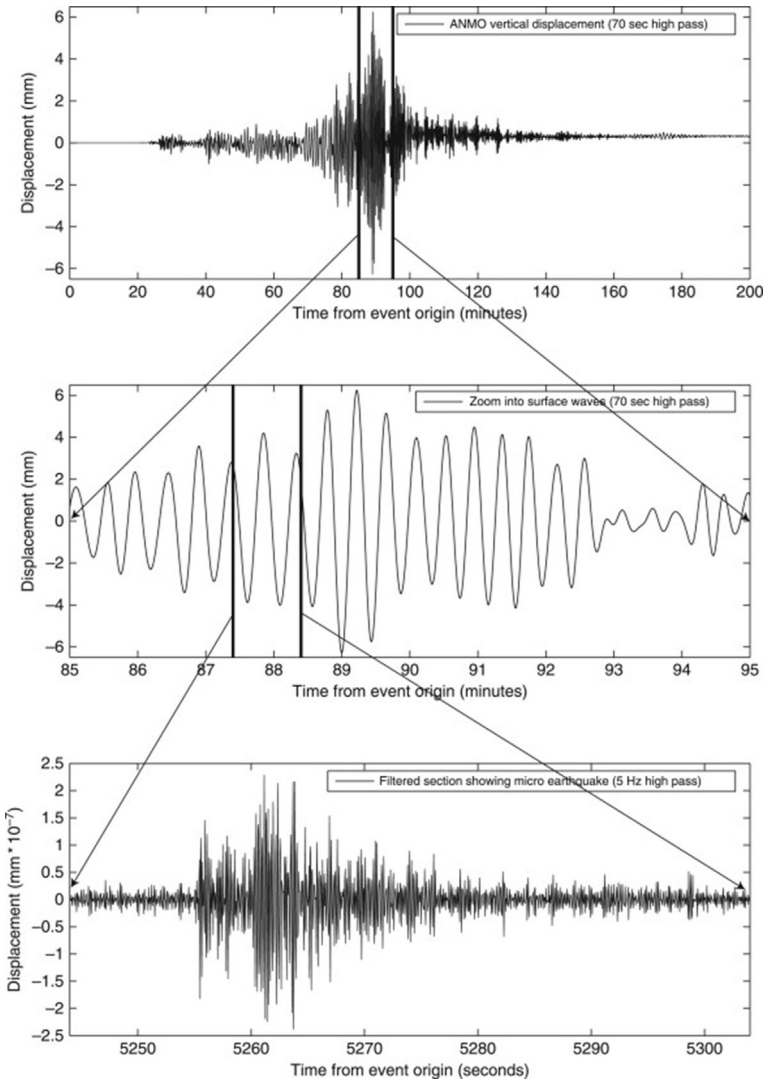

Figure 14 Illustration of the dynamic range of a VBB station (ANMO). A recording of a local microearthquake with magnitude below 1 is extracted from the record dominated by the minor-arc surface waves generated by the 2004 Sumatra–Andaman magnitude 9.3 event. Reproduced from Park J, Butler R, Anderson K, et al. (2005) Performance review of the global seismographic network for the Sumatra–Andaman megathrust earthquake. *Seismological Research Letters* 76 (3): 331–343.

2000 deployments for up to 2 years in a given location; the average instrument spacing is 70 km. In 2013, it has reached the East Coast and preparations are under way to redeploy about half of the instruments in Alaska. The 'reference array' provides the means to relate the waveforms recorded at different stages of TA deployment. Many other portable networks for regional studies of the crust and lithosphere using passive and active sources have been developed and deployed in the last 20 years (see Chapters 1.11, 1.16, and 1.17).

1.01.4 Current Issues in Global Tomography

In parallel with instrument development, scientific progress in seismic tomography has been rapid during the last 20 years, and most of the accomplishments are summarized in two reviews by Romanowicz (1991) and Romanowicz (2003), as well as in Chapters 1.10 and 1.19. However, there are still issues that remain unresolved or controversial. Certainly, there are confusing observations related, for example, to anisotropic properties or differential rotation of the inner core, the core–mantle topography, anticorrelation of density and shear velocity near the bottom of the mantle, the strength and depth distribution of anisotropy in the Earth's mantle, the presence of the postperovskite phase at the base of the mantle, and its role in mantle dynamics.

But the foremost issue in our view relates to the derivation and interpretation of 3-D Earth models. We will mention three issues in particular: parameterization, datasets used for model construction, and theoretical assumptions.

Ever since it was discovered that inversion of ill-conditioned matrices can be dealt with by requiring minimization of the norm or roughness of the model, we have been obtaining models whose reliability is difficult to assess.

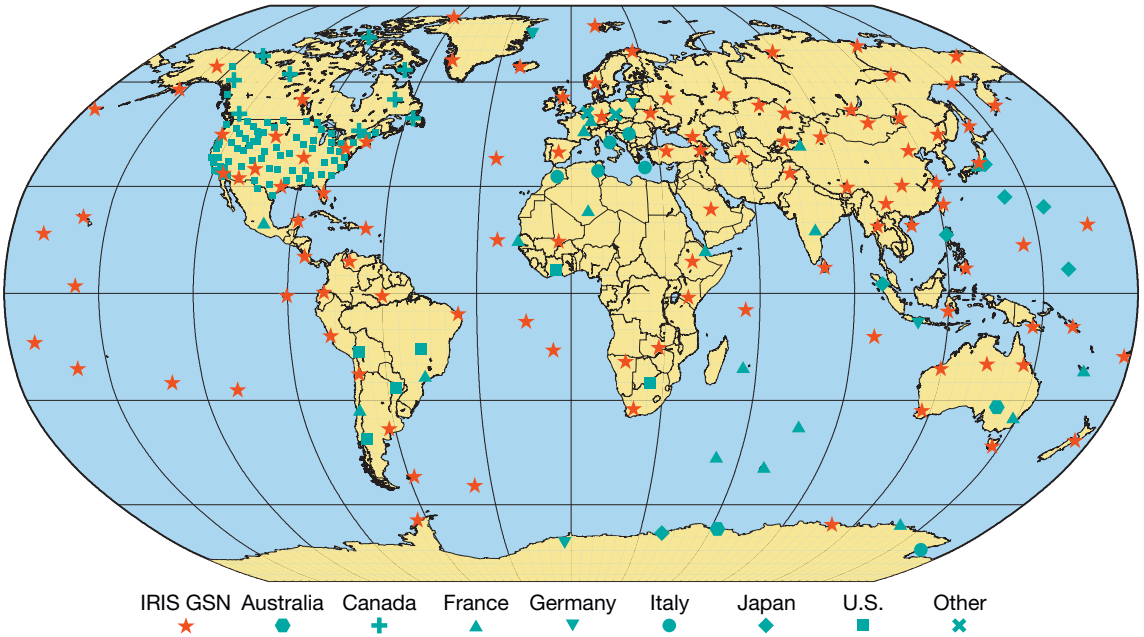

Figure 15 Current (January 2014) map of the stations of the Federation of Digital Seismographic Networks. Stations of different member networks are identified by symbols shown at the bottom. Courtesy of Andy Frassetto (IRIS Instrumentation Services).

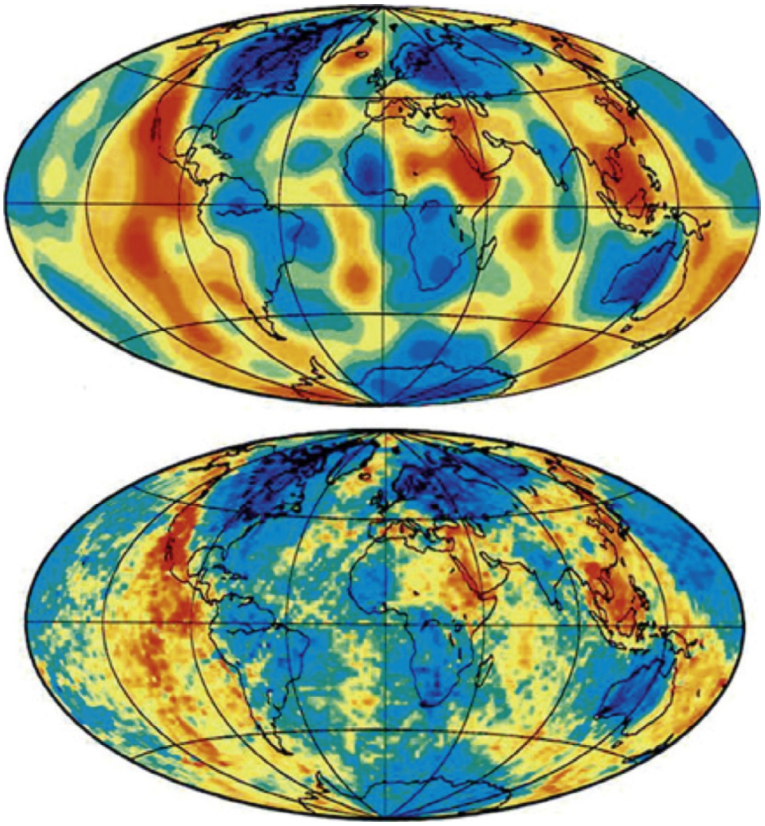

Figure 16 Demonstration of the results of inversion of the same data set (40 000 phase-delay data for 75 s Rayleigh waves measured by Ekström et al., 1997) for different numbers of parameters. The top map shows inversion for spherical harmonic coefficients up to degree 16 (289 parameters). The bottom map shows the results of inversion for about 10 000 equal-area blocks; in this case, matrix conditioning is necessary. The amplitude of the anomalies is lower, artifacts of an uneven path distribution are visible (e.g., across the central Atlantic), and it is difficult to find features that have not been resolved by the top map. The conclusion is that there is a price for unduly increasing the number of unknowns. Courtesy of L. Boschi.

Figure 16 illustrates an example of how the results can be altered with the change of parameterization. A set of about 40 000 phase-delay data for Rayleigh waves with 75 s period (Ekström et al., 1997) are inverted for 'local' phase velocities. The top panel of Figure 16 shows the result in which the data were inverted for a set of basis functions represented by spherical harmonics up to degree 16; this requires solving for 289 unknown coefficients. Because the data set is so large and the global coverage is good, the solution was obtained by an exact matrix inversion. The results look reasonable, without any indication of instability. The lower panel of Figure 16 shows the result obtained using a $2^\circ \times 2^\circ$ block expansion, which requires solving for approximately 10 000 unknown values. Matrix conditioning was required in this case, and it was accomplished by applying combined norm and roughness damping. What is clear from the 'high-resolution' solution is that the amplitudes are generally lower and there are 'streaks' indicating artifacts caused by uneven sampling of the area. What is difficult to find, however, are any features that appear to be significant that are not present in the solution with 30 times fewer parameters. Thus, sometimes, less is better. There is no absolute rule; as discussed in the previous section, the answer depends on the character of power spectra of a particular function.

The issue of parameterization is an important one, particularly if the global behavior of the solution is to be preserved. Figure 17 illustrates cross sections of four global P-velocity models – derived from the same data source (ISC Bulletins) – that span three orders of magnitude in the number of parameters. Clearly, there is not a simple relationship between the number of parameters and information contained in the model. It is so, partly, because the lower-mantle spectrum is dominated by the very low degrees that are well recovered by the degree-6 model.

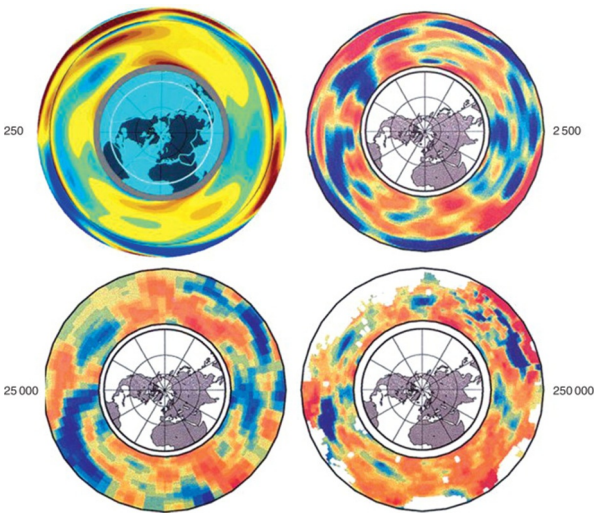

Figure 17 Comparison of the equatorial cross sections of four P-velocity models obtained by inversion of travel-time residuals from ISC Bulletins using a number of unknown parameters that span three orders of magnitude. The image of the African and Pacific superplumes is clearly seen in the model derived by using 250 parameters, while it could not be readily inferred from the model that used 250 000 parameters. The models obtained using 2500 and 25 000 parameters support the conclusion drawn from discussion of Figure 16. Modified from Boschi L and Dziewonski AM (1999) 'High' and 'low' resolution images of the Earth's mantle – Implications of different approaches to tomographic modeling. *Journal of Geophysical Research* 104: 25567–25594.

1.01.4.1 Resolving Power of Datasets Used for Constructing Models

Another important issue in assessing global, as well as regional, tomographic models is the data set (or subsets) and the resolving properties that were used to derive them. The mantle models derived using only teleseismic travel times, for example, have very little radial resolution in the upper mantle, because the ray paths do not bottom there. The teleseismic travel times are sensitive to velocity perturbations in the upper mantle, but the variations with radius cannot be satisfactorily resolved above the lower mantle. For example, all maps of upper-mantle velocity anomalies in Figure 18 show that a model derived using only teleseismic travel times has slow velocities under mid-ocean ridges at all upper-mantle depths, simply from the smearing with depth of the large slow anomalies occurring near the surface. This is a result of norm damping in a situation where sampling is inadequate: a compromise between fitting the data and having a low norm (low sum, or integral, of squared model perturbations). The spreading centers and cratons have largest signal in the uppermost 250 km of the upper mantle; the variance in the next

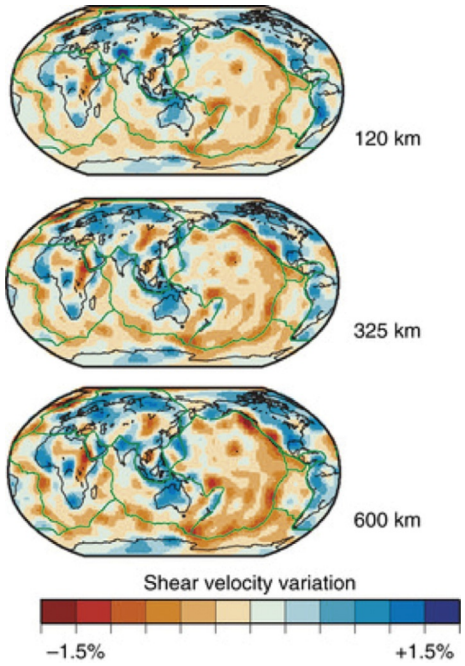

Figure 18 A fragment of a figure from Ritsema et al. (2004) illustrating a typical result of an upper-mantle structure obtained using teleseismic travel times, whose rays do not bottom in the upper mantle. The three maps show smeared-out structure from near the top of the mantle (mid-ocean ridge anomalies). The conclusion drawn from the full figure (see Chapter 1.10) is that, to obtain a whole-mantle model, one should use diverse types of data. Modified from Ritsema J, van Heijst HJ, and Woodhouse JH (2004) Global transition zone tomography. *Journal of Geophysical Research* 109: B02302, http://dx.doi.org/10.1029/2003JB002610.

400 km is an order of magnitude less. Thus, the minimum norm compromise leads to the smearing of the shallow structure over the entire upper mantle (for positive integers, $l+m+n=3$ has the minimum norm solution (1, 1, 1) with the norm of 3, the 'true' solution (3, 0, 0) has a norm of 9, and an intermediate solution (2, 1, 0) has a norm of 5). Another way to accommodate the minimum norm compromise is to make the upper-mantle model small; there are published models derived using only teleseismic travel times that have heterogeneous structure in the upper mantle with very small amplitude.

Models built using teleseismic travel times and fundamental-mode dispersion data do not have sufficient resolution in the transition zone to distinguish its unique properties. So far, only three research groups involved in whole-mantle modeling (Michigan/Oxford, Berkeley, and Harvard) use data allowing sufficient resolution in this region; it is interesting that they obtain these models using different kinds of data and theories, therefore adding to the credibility to the results. The use of waveforms in deriving 3-D models was pioneered by Woodhouse and Dziewonski (1984), but in the original paper, only data with periods longer than 135 s were used. Long-period body waves were used in inversions by Woodhouse and Dziewonski (1986) and Woodhouse and Dziewonski (1989). Dziewonski and Woodward (1991) combined waveforms and teleseismic travel times measured by Woodward and Masters (1991). The immediate result was that the two models they derived showed a sudden change in the pattern of heterogeneities across the 670 km boundary, and this was pointed out and discussed by Woodward et al. (1994). Later inversions by the Harvard group included also surface-wave dispersion data reported by Ekström et al. (1997). This increased resolution near the surface but did not alter the behavior across the upper–lower mantle boundary (Gu et al., 2001, 2003; Kustowski et al., 2008). All these models were obtained using the path average approximation (PAVA), which assumes constant average structure along the great-circle path connecting the source and the receiver. The Berkeley group pioneered use of a more advanced theory called nonlinear asymptotic coupling theory (NACT) first described by Li and Romanowicz (1995) and based on the across-branch coupling asymptotic development of Li and Tanimoto (1993). This theory allowed them to construct body-wave kernels that give good representation of the sensitivity along and around the ray path as shown in **Figure 19** and therefore opened the way to tomographic inversions for whole-mantle structure based entirely on waveform data and thus exploit more information in the seismograms than can be achieved with only those phases that are well separated from others in teleseismic records. In applying NACT to the development of several generations of global mantle models (Li and Romanowicz, 1996; Mégnin and Romanowicz, 2000), most recently including attenuation (Gung and Romanowicz, 2004) and radial anisotropy (Panning and Romanowicz, 2006), the Berkeley group divided the seismograms into wave packets containing one or several body waves or surface-wave overtones, which allowed them to weigh different phases differently in order to obtain uniform sensitivity with depth. The Berkeley group does not use travel times explicitly, but information on structure is included in the phase of a waveform of, for example, an SS-arrival. Thus, a large collection of waveforms containing

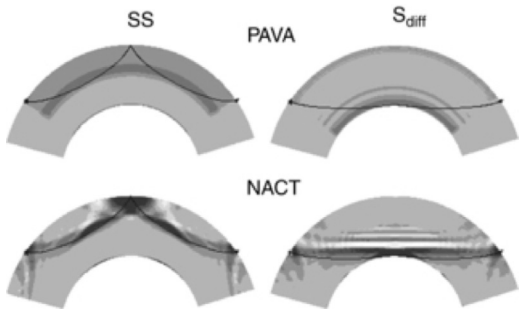

Figure 19 Comparison of sensitivity kernels in the vertical plane containing the source and the receiver for SS waves (left) and S_{diff} waves (right), using the path average approximation (PAVA, top) and the nonlinear asymptotic coupling theory (NACT, bottom). PAVA produces 1-D kernels, which do not represent well the ray character of body waves. NACT, which includes across-branch mode coupling, produces 2-D finite-frequency kernels that more accurately represent the sensitivity along and around the ray path as well as its variations with position along the ray. Because this is a time domain formalism, the NACT kernels are time-dependent and are here represented at a particular point in the waveform, with positive maxima in black and negative ones in white. Shadows beyond the source and receiver are due to the truncation in the coupling series. Adapted from Li XD and Romanowicz B (1995) Comparison of global waveform inversions with and without considering cross branch coupling. *Geophysical Journal International* 121: 695–709.

images of phases such as S, SKS, S_{diff}, Love, and Rayleigh fundamental and overtone waves will represent similar information as the combination of teleseismic travel times and surface-wave phase velocities in the Caltech/Oxford or Harvard models. In addition, unlike travel-time analysis, wave packets containing several phases with close arrival times but different sampling of mantle structure can be included, improving resolution. An important element of the data set used by Ritsema et al. (1999) is a set of maps of Rayleigh wave overtone dispersion from the first to the fifth overtones. These were obtained by 'stripping' the seismograms of subsequent overtones, thus providing the data on the average phase velocity of a particular overtone between the source and the receiver (van Heijst and Woodhouse, 1997). Since body waves represent superposition of overtones, use of complete waveforms is, to a large extent, equivalent; however, the separation of data for individual overtones allows assignment of different weights to different overtones, while direct waveform methods use them with the weight that is determined by their excitation; generally, the amplitude of overtones decreases with the overtone number. On the other hand, waveforms contain information about all the overtones. The importance of the overtones (body-wave waveforms) was shown implicitly by Gu et al. (2001) and explicitly by Ritsema et al. (2004). The importance of using adequate kernels for overtone and body waveforms was illustrated by Mégnin and Romanowicz (1999) in a comparison of the PAVA and NACT inversion approaches.

1.01.4.2 Theoretical Assumptions

Ray theory vs. finite-frequency theory has been the subject of a lively debate within the seismological community during the last decade. Much of it has revolved around the

'banana–doughnut' kernels (Dahlen et al., 2000) and its application to mantle modeling (Montelli et al., 2004a,b). The implication conveyed by those authors was that the results obtained using finite-frequency theory were distinctly superior to those obtained using ray theory. The serious implication of this was that all tomographic studies to date were deficient. Yet, a direct comparison of the finite-frequency and ray theory models published by Montelli et al. (2004b, Figure 9) demonstrates that the two models are nearly identical, save for a scaling factor of 1.14 (van der Hilst and deHoop, 2005). This is because these authors introduced finite volume parameterization by tetrahedra with unknown velocity perturbations at the vertices (with linear interpolation within each tetrahedron) without acknowledging that this is equivalent to a low-pass filtration.

There have been quite a few papers published on this subject (e.g., Peter et al., 2007). While it is obviously desirable to use a more accurate theory, it is worthwhile to investigate why the ray theory and finite-frequency theory yield nearly identical results. A particularly clear explanation of this effect is presented by Dalton (2007) who used the orthogonal basis functions (spherical harmonics) for both the kernels and velocity perturbation, with the phase velocity model truncated at degree L. A perturbation in phase travel time between source located at s and receiver at **r** can be calculated by integration over the surface of the sphere Ω:

$$\delta t_{s,r} = \int_{\Omega} \frac{\delta v}{v_0}(\theta, \varphi) K^{s,r}(\theta, \varphi) \mathrm{d}\Omega \qquad [1]$$

where v_0 is the reference velocity and $K^{s,r}(\theta,\phi)$ is the kernel calculated for a particular location of the source and the receiver. Expanding δv and $K^{s,r}(\theta,\phi)$ in spherical harmonics and truncating expansion of δv at $l=L$, we have

$$\delta t_{s,r} = \int_{\Omega} \left(\sum_{l=0}^{l=L} \sum_{m=-l}^{m=+l} \delta v_{l,m}/v_0 Y_{l,m}(\theta, \varphi) \mathrm{x} \right) \cdot \left(\sum_{l'=0}^{l'=\infty} \sum_{m=-l'}^{m'=+l'} K^{s,r}_{l',m'} Y_{l',m'}{}^{*}(\theta, \varphi) \right) \mathrm{d}\Omega \qquad [2]$$

However, because of the orthogonality of spherical harmonics, this reduces to

$$\delta t_{s,r} = \sum_{l=0}^{l=L} \sum_{m=-l}^{m=+l} \delta v_{l,m}/v_0 K^{s,r}_{l,m} \qquad [3]$$

with the terms in expansion of the kernel function for $l' > L$ having no effect.

Figure 20 (*top*) shows the frequency-dependent kernels for Love waves at 35 and 200 s period. In the *middle*, there is the frequency-dependent kernel expanded to degree 18. At the bottom is the spherical harmonic expansion of a line ('ray theory') along the equator $K=\delta(\theta-\pi/2)$ for $\phi>0$ and $\phi<\Phi$ and zero elsewhere. At the period of 35 s, it is difficult to tell the difference between the *middle* and the *bottom* 'effective' kernel functions. The difference is still quite small at 200 s period. Thus, finite parameterization can imitate the finite-frequency effect, and for relatively low L, the advantage of using the finite-frequency kernels vanishes. Dalton showed that differences are more pronounced at larger L, but the earlier discussion indicates that there is very little power in the higher degrees of $\delta v_{l,m}$ and the effect on the observed, or computed, $\delta t_{s,r}$ will be insignificant because of 'natural truncation.' Thus, under the circumstances presented here, the effect of using finite-frequency kernels is very small. In general, the ratio of the width of the finite-frequency kernel to the path length

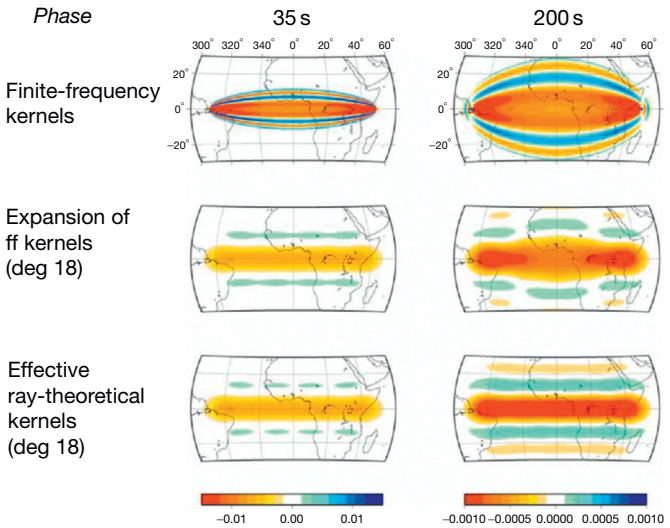

Figure 20 Demonstration of the perhaps counterintuitive fact that 'finite-frequency' kernels and 'ray theory' kernels may lead to very similar models if the model to be obtained using 'ray theory' is parameterized. Parameterization using spherical harmonic expansion up to a maximum order L is used here, because the result is exact. *Top*: Born (finite-frequency) kernels for the phase travel-time delay for Love waves at 35 s (left) and 200 s (right). *Middle*: Synthesis of the Born kernels above obtained by synthesis of spherical harmonic coefficients up to degree $L=18$. The spherical harmonic coefficients for $l>18$ are irrelevant because of the orthogonality of the basis functions. *Bottom*: Expansion of a 90° long ray up to the same $L=18$. The effective kernels for 35 s waves are difficult to distinguish from the expanded finite-frequency kernels; the differences are more noticeable at 200 s period but they are still minor.

determines how good the ray theory approximation is; finite-frequency kernels can be important in regional-scale studies.

Indeed, as discussed earlier, the possibility of inverting complete seismograms (i.e., seismic waveforms) without selecting individual phases for travel-time measurements opens the way for exploiting more of the information contained in the recorded wavefield, thereby achieving better sampling of the mantle. In particular, we note that models based entirely on the inversion of time domain waveforms are able to achieve comparable results, with an order of magnitude fewer records (e.g., a total of 20 000 records in Panning and Romanowicz, 2006) as models based on the standard combination of surface-wave dispersion and body-wave travel times, which typically use tens to hundreds of thousands of measurements. This is because the smaller number of source-station paths considered is compensated by the inclusion of waves that sample mantle structure in a richer variety of ways.

Since our ability to improve the global distribution of sources and receivers is limited, once it is recognized that waveform inversion represents potential for better sampling of the Earth's mantle, the attention then shifts to improving the methods of computation of synthetic seismograms in a 3-D Earth.

NACT (Li and Romanowicz, 1995) provided a successful theoretical approach for this purpose and has led to several generations of whole-mantle shear velocity models in the last 20 years. However, asymptotic normal-mode perturbation theory is only valid for Earth models for which the wavelength of the structure is large compared to that of the seismic waves considered (i.e., smooth models) and heterogeneity is weak (nominally, lateral variations of up to ~10%). Yet, in the Earth's boundary layers, that is, in the upper mantle and in the D″ region, there is ample evidence for the presence of stronger heterogeneity, whereas throughout the mantle, heterogeneity at many different scales may be present. First-order mode perturbation theory is not appropriate in this case. While higher-order perturbation theory has been worked out (e.g., Lognonné and Romanowicz, 1990; Lognonné, 1991), it is cumbersome for use in practice, in particular because it always requires a 1-D reference model.

In the last decade, advances in numerical methods for the computation of the seismic wavefield in arbitrary 3-D structures, and increased computational power, have made it possible to replace normal mode-based synthetics by more accurate ones, based on the spectral element method (SEM), first introduced in global seismology by Komatitsch and Vilotte (1998) and later perfected by Komatitsch and Tromp (2002). The use of SEM has now been implemented in tomographic inversions for crustal structure at the local scale (e.g., Tape et al., 2010) and upper-mantle structure at regional scales (e.g., Fichtner et al., 2009; Rickers et al., 2013; Zhu et al., 2012). The forward numerical computation is generally combined with an 'adjoint' numerical computation of the kernels for inversion (e.g., Tromp et al., 2005; see **Chapter 1.07**) or, alternatively, with a 'scattering integral formalism' (e.g., Chen et al., 2007). Still, computational time increases as the third power of frequency, so the computational challenge limits the frequency range of computations to relatively long periods (typically longer than 40 or 50 s), especially when using the adjoint framework, which requires many iterations (sometimes 20–30) due to the slow convergence of the conjugate-gradient method.

Because the teleseismic wavefield needs to be computed for a long time interval, in order to include all seismic phases of interest (up to and including second orbit fundamental-mode Love and Rayleigh waves), the use of the SEM for global tomography is particularly challenging computationally. The first global shear velocity models developed using SEM (French et al., 2013; Lekic and Romanowicz, 2011) are limited to the upper mantle due to the use of relatively long periods (longer than 60 s) for computational efficiency. To reduce further computation time, they take advantage of efficiencies gained, in the forward step of the computation, by restricting the numerical computation to the mantle through coupling with 1-D mode computations in the core (CSEM, Capdeville et al., 2003) and replacing the finely layered crust by an equivalent smooth crust constrained by surface-wave dispersion data. In the inverse step, the kernels, which do not need to be as accurate as the forward predictions (e.g., Lekic and Romanowicz, 2011; Tarantola, 2005), are calculated using a mode-based approximation. The use of a Gauss–Newton formulation of the inverse problem leads to much more rapid convergence than the adjoint approach. The use of accurate wavefield computations, such as afforded by SEM, is particularly important to improve resolution of low-velocity regions, which tend to be hidden from observation, when ray theory is used, due to wave front healing effects (e.g., Nolet and Dahlen, 2000). For example, the new-generation tomographic models based on the use of SEM resolve the minimum amplitude of the upper-mantle low-velocity zone better than previously, even in areas far away from sources and stations, as illustrated in **Figure 21**, and are starting to resolve finer details of the 'plumbing' system in the oceanic upper mantle (e.g., Colli et al., 2013; French et al., 2013; Rickers et al., 2013).

1.01.4.3 Robust Features of Current Global Mantle Models and Their Implications

The full impact of the completed FDSN network, progress in automatic processing of data – measurements of travel times from waveforms or selection of time windows for waveform inversion, for example – improved the database by an order of magnitude in comparison with earlier models. This has been accompanied by better recognition of what is required to obtain a stable 3-D model of shear velocity anomalies in the mantle. Among these are as follows:

(i) Assembly of data that are sensitive to structure from the Moho to CMB; usually, this calls for a combination of surface-wave dispersion, overtones, and teleseismic travel times.
(ii) Proper weighting of the subsets of data to assure comparable radial resolution.
(iii) Careful selection of matrix stabilization parameters.
(iv) Even though gaps in coverage due to the uneven distribution of sources and receivers are unavoidable, it is desirable to minimize the impact of this inequality. For example, Dziewonski (1984) used a form of a 'summary ray' approach, counting the number of rays connecting a particular 'receiver cell' and 'source cell' (each $5° \times 5°$ at the equator) and then counterweighed individual

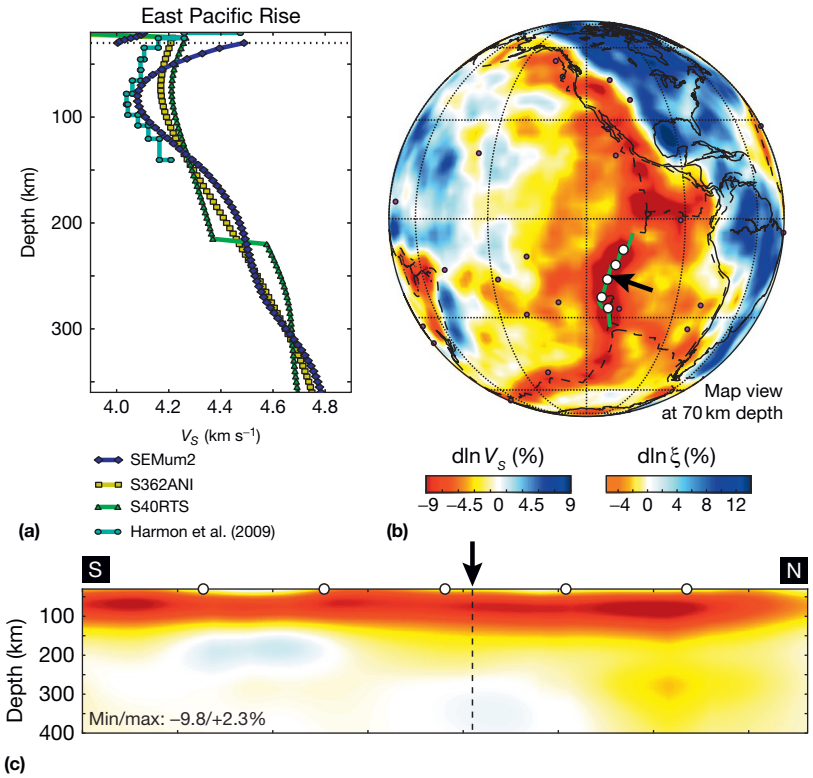

Figure 21 Isotropic V_S structure beneath the East Pacific Rise (EPR). (a) A comparison between the mean 1-D V_S profile obtained from the high-resolution OBS-based tomographic study of EPR structure by Harmon et al. (2009) and that sampled from global models SEMum2 (French et al., 2013), S362ANI (Kustowski et al., 2008), and S40RTS (Ritsema et al., 2011), in the same location. The 1-D profile of the Harmon et al. study was obtained from a harmonic mean of the central portion of their model over length scales consistent with the a priori correlation lengths employed in the SEMum2 inversion (~400 km). SEMum2 more closely recovers the strength and depth of the low-velocity zone (LVZ) beneath the EPR inferred from the local study than either of the other global models. (b) Relative variations in isotropic V_S structure at 70 km depth in SEMum2, focused on the EPR, showing both the location of the comparison in (a) (black arrow) and the extent of the ~3750 km line of section in (c) (portion of EPR highlighted in green). (c) A cross section along the EPR, following the green line and white dots shown in (b), illustrating the strength and extent of the strong low-velocity anomaly imaged beneath the EPR in SEMum2 (c), nearly −10%. Black arrow and dashed line indicate approximate location of profiles in (a). Reproduced from Figure S6 of French S, Lekic V, and Romanowicz B (2013) Waveform tomography reveals channeled flow at the base of the oceanic asthenosphere. *Science* 342: 227–230.

observations such that impact of a given pair of cells was equal regardless of the number of connections. Since there were about 25% of pairs with only one connection and only 25% had more than ten connections, the variance reduction was very modest.

Figure 22 compares model S40RTS (Ritsema et al., 2011) at seven different depths with four other relatively recent models: S362ANI (Kustowski et al., 2008), SAW642AN (Panning and Romanowicz, 2006), TX2008 (Simmons et al., 2009), and HMSL-S (Houser et al., 2008). The data sets used to derive each of these models were different; even the theories used were different. Therefore, their overall similarity (with one exception) indicates congruence of the global 3-D models of the whole mantle. There are differences, of course, and some of them should be resolved, but the 'big picture' is robust and its implications should be considered in modeling the global mantle flow. Such modeling is necessary to understand mantle dynamics and evolution, since tomography can retrieve only the present-day picture. What makes the work of Ritsema et al. (2011) particularly important is that the data set used in this inversion is an order of magnitude greater than in their earlier model S20RTS (Ritsema et al., 1999) and, yet, the differences between the two models are small, especially at larger wavelengths. This means that the features within the 'red' part of the spectrum are well resolved and further increase in the data set will not change the image appreciably at long wavelengths.

There is a fundamental similarity among the models; all show an order of magnitude decrease in power between 100 and 400 km depth (the scale for the top row of maps is ±7%, or 3.5 times larger than at other depths). While the dramatic difference between the maps at 600 and 800 km is distinct for the first three models, it is less so for the last two; the explanation is that models TX2008 and, especially, HMSL-S did not use enough data with resolution in this depth range to map properly this critically important feature. The rms amplitude is the lowest between 650 and 1800 km depth but then increases again to reach the maximum at the CMB.

The power spectrum as a function of depth and wave number is a robust feature (see Figure 9 in Kustowski et al., 2008). On this basis, it is possible to distinguish several depth regions with different spectral characteristics; Dziewonski et al. (2010)

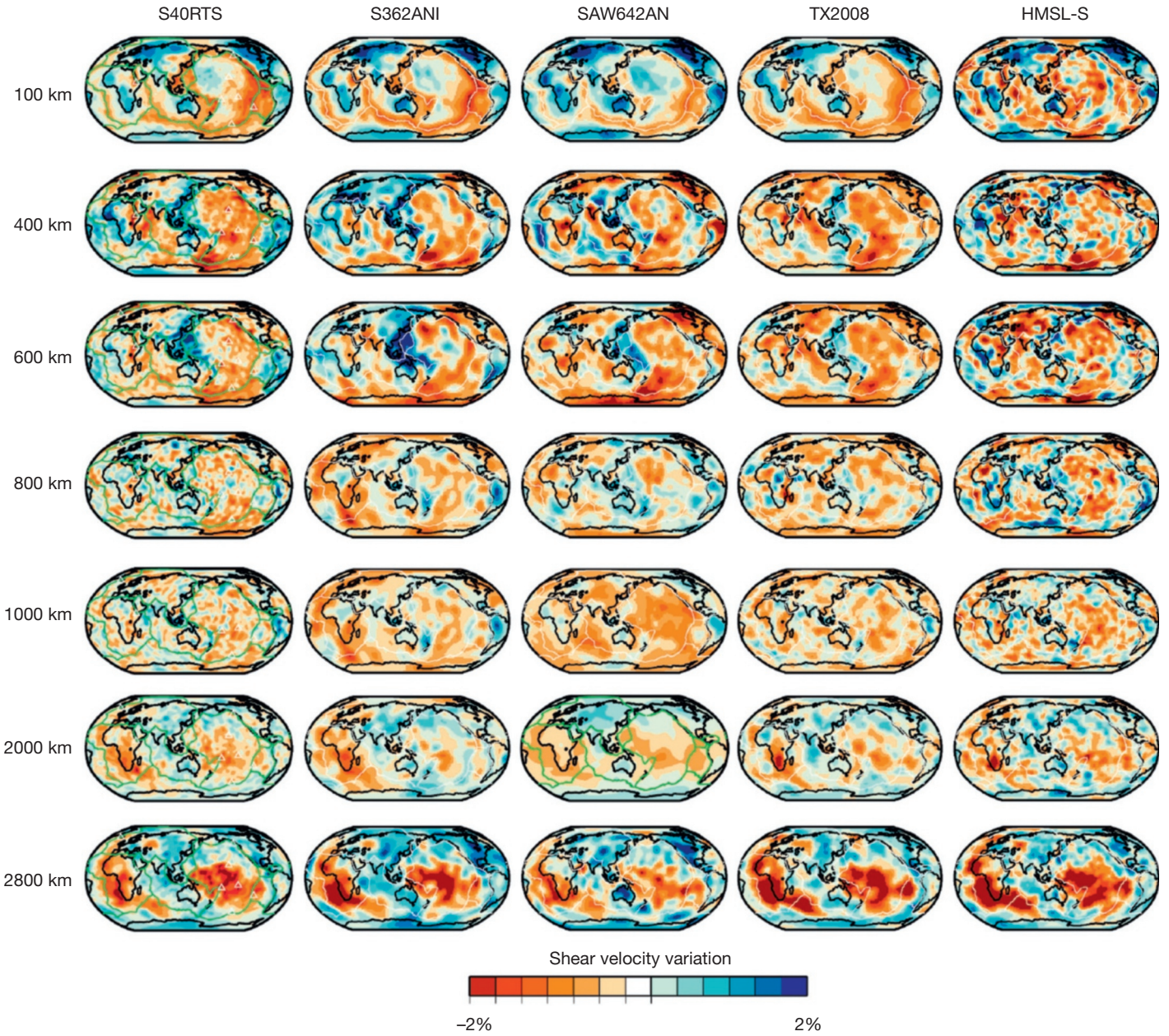

Figure 22 Comparison of shear velocity maps at depths of (from top to bottom) 100, 400, 600, 800, 1000, 2000, and 2800 km for models (from left to right) S40RTS (Ritsema et al., 2011), S362ANI (Kustowski et al., 2008), SAW642AN (Panning and Romanowicz, 2006), TX2008 (Simmons et al., 2009), and HMSL-S (Houser et al., 2008). The velocity varies from −2% to +2% from the average value. Shear velocity perturbations are between −7% and +7% from the average value for the map at 100 km depth. Reproduced from Ritsema J, Deuss A, van Hejst HJ, and Woodhouse JH (2011) S40RTS: A degree-40 shear-velocity model for the mantle from new Raleigh wave dispersion, teleseismic traveltime and normal-mode splitting function measurements. *Geophysical Journal International* 184: 1223–1236, http://dx.doi.org/10.1111/j.1365-246X.2010.04884.x.

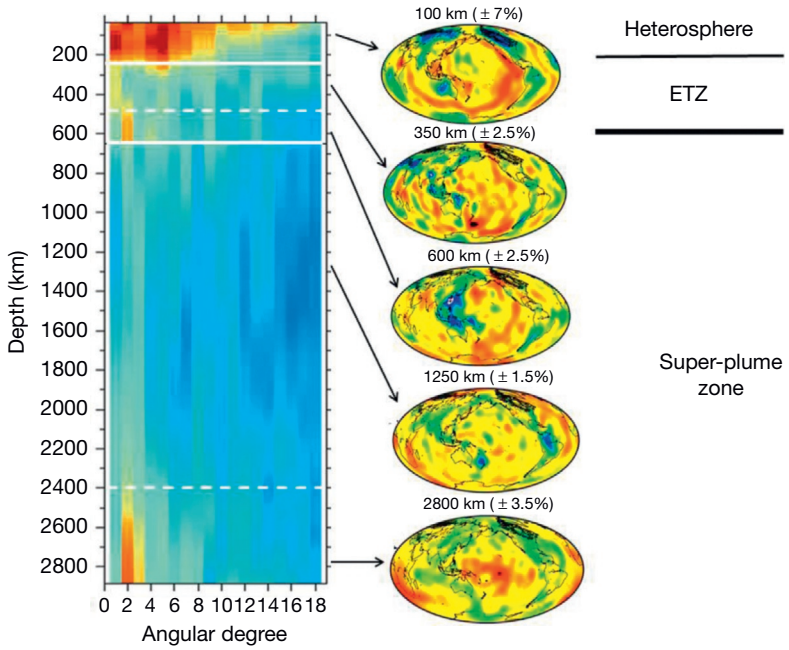

Figure 23 *Left:* Power spectrum of model S362ANI of Kustowski et al. (2008) as a function of harmonic degree and depth. Continuous white lines indicate inferred major divisions in spectral characteristics; broken white lines show additional subdivisions. *Center*: Maps of shear velocity anomalies at depths 100 km (±7%), 350 km (±2.5%), 600 km (±2.5%), 1250 km (±1.5%), and 2800 km (±3.5%). *Right*: Schematic division of the mantle into three zones with profound changes at their boundaries: 'heterosphere' with a very high level of heterogeneity; 'extended transition zone,' with a weak, white spectrum at the top and power shifting to degree 2 above the 650 km discontinuity; and 'superplume zone' dominated by degrees 2 and 3, which is strongest at the CMB but continuing with decreasing amplitude throughout the entire lower mantle.

proposed five such regions; more recent analysis (Dziewonski et al., 2013) finds that these can be combined into three principal zones.

Figure 23 shows the power spectrum of model S362ANI with maps of shear velocity anomalies at five different depths. The principal divisions are between the 'heterosphere' (HS, Moho – 250 km depth), the 'extended transition zone' (ETZ; 250–650 km), and the lower mantle or 'superplume zone' (SPZ). The spectrum changes gradually within the ETZ from white to being dominated by degree 2, but this change is not sudden and is not associated with the 410 km discontinuity. In the SPZ, there is a change in the gradient of heterogeneity at about 2400 km depth (e.g., Lekic et al., 2012), but the pattern does not change. These two more subtle spectral changes are shown with broken lines; the fundamental ones - with continuous lines.

Comparison of the five maps shows that the heterogeneity is distinctly different in each zone or subzone. 'Heterosphere' is dominated by surface tectonic features: slow ridges, cooling plates, and fast cratons. Between 150 and 250 km depth, the power of heterogeneity decreases by an order of magnitude, hence the name.

Below 250 km, the upper part of the ETZ is characterized by a nearly white spectrum. Oceans, particularly Pacific, are slow but do not show the age signature; continental structure tends to be faster than average, but the location of the anomalies is not as closely associated with the cratons as at 100 km depth. Between 450 and 650 km depth, the degree-2 anomalies become dominant. Regional-scale studies such as Fukao et al. (1992, 2001, 2009), Fukao and Obayashi (2013), and **Chapter 1.20** as well as global scale of Gu et al. (2001, 2003) explain this by stagnation above the 650 km discontinuity of the recently subducted slab, which appears to lay flat at the bottom of the transition zone for sometimes as far as 2000 km. This is consistent with the already discussed pattern of abrupt change of shear velocity anomalies at depths of 600 and 800 km for the first three models in Figure 22.

At the top of the 'superplume planet' in the mid-mantle, the signal is weak and has a somewhat flat spectrum, even though the degrees 2 and 3 have the largest power. The amplitude of anomalies begins to increase below 1800 km depth. In the 'abyssal layer' (2400 km – CMB), degrees 2 and 3 are clearly dominant and show the pattern of two superplumes (African and Pacific) separated by a wide circumpolar ring of higher than average velocities. This pattern of zero line is very robust, as shown by Lekic et al. (2012).

Figure 24 shows the result of cluster analysis of the deepest 1000 km of the mantle of the five models shown in Figure 22. On a constant area $2^\circ \times 2^\circ$ grid, the average velocity anomaly for a particular model is classified as either 'slow' or 'fast'; if it is slow, integer 1 is added to the voting map and 0 if it is fast. If all models are 'slow' at a given grid point, the corresponding color is deep red; if all models are fast, then deep blue. The robustness of this classification is demonstrated by the fact that over 95% of the area is either deep red or dark blue. The other important inference is that even though the individual models show variations in amplitude, these do not lead to the change in sign of the anomaly: the dark red and dark blue regions are contiguous. One exception is a distinctly separated 'slow' anomaly, which Lekic et al. (2012) named the 'Perm anomaly' because of the proximity of its surface projection to the city of Perm (Russia). Another possible exception is a larger area beneath the East Pacific Rise, but the models are not

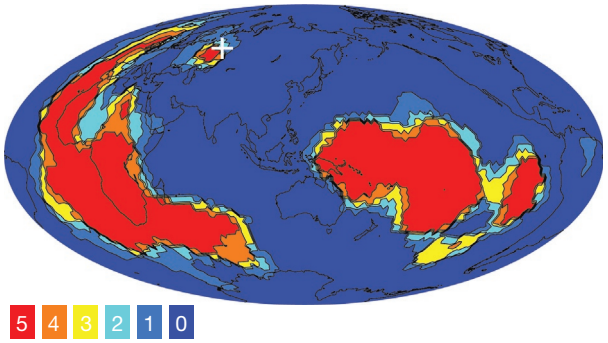

Figure 24 Cluster analysis of shear velocity (V_s) profiles (1000–2800 km depth range) from five recent global tomographic models (Houser et al., 2008; Kustowski et al., 2008; Mégnin and Romanowicz, 2000; Simmons et al., 2010; Ritsema et al., 2011) in the lower mantle defines two regions whose geographic extents are consistent across models, tracing out the African and Pacific superplumes, as well as a single, globally contiguous faster-than-average region. Pixels that make up this map are color-coded according to how many models assign the V_s profile beneath that point to the slow cluster. The models are spatially filtered to exclude power at spherical harmonic degrees $\ell > 18$. Reconstructed location (Torsvik et al., 2008) of the center of Siberian Trap eruptions is indicated by the white cross. Reproduced from Lekic V, Cottaar S, Dziewonski A, and Romanowicz B (2012) Cluster analysis of global lower mantle tomography: A new class of structure and implications for chemical heterogeneity. *Earth and Planetary Science Letters* 357–358: 68–77.

unanimous here. The white cross indicates the location of the Siberian Traps 250 Ma ago by Torsvik et al. (2008).

In order to put the Perm Anomaly on the map, it is necessary to synthesize the first 12 harmonics of the expansion of the map shown in **Figure 24** (see Figure 7 in Lekic et al., 2012). The significance of the unanimity of all five models is that we can resolve the structure near the CMB to about 1000 km half-wavelength. This confirms the conclusion that degree-2 and degree-3 anomalies are real features rather than a result of insufficient data to resolve smaller-scale structures. Another conclusion is that there is a dichotomy between the planetary-scale structures (superplumes) and smaller-scale anomalies, such as ULVZs or hypothetical narrow plumes. It is not clear, therefore, that the latter structures play a predominant role in whole-mantle dynamics. On the other hand, the superplume pattern continues upward to the middle mantle. Figure 3 in Lekic et al. (2012) shows that the voting pattern of **Figure 24** continues into the middle mantle; even though the signal-to-noise ratio is considerably lower in the 800–1800 km depth range. The superplume pattern is distinct and contains all the surface locations of hot spots; also, the band of faster-than-average velocities continues to maintain its width, indicating that the fundamental pattern of velocity anomalies continues throughout the lower mantle, although with decreasing amplitude.

A by-product of the voting procedure is the derivation of average fast and slow velocity anomalies for each of the all five models (see Figure 5 of Lekic et al., 2012). There are two important conclusions that can be drawn from this comparison. First, the slow anomalies are about three times stronger than the fast ones; this is consistent with the fact that in **Figure 24**, the area of 'blue' is much larger than that of 'red.' Second, there is a sharp change in the gradient of the velocity anomalies at about 500 km from the CMB, above which it becomes much shallower. It is possible to speculate that the steep gradient in the lowermost mantle is due to a chemical heterogeneity whose strength decreases with radius to reach that of the ambient mantle 500 km above the CMB. Further, it would be possible to modify the 'average' Earth model by adding a small 1-D linear increase of velocities between 1600 km depth and the CMB, where it would amount to 0.5%. If this were then subtracted from the 3-D model, the map of anomalies in the abyssal zone region would be mostly limited to slow anomalies, such that with this modification, the principal anomalies would be limited to superplumes. Thus, the chemical heterogeneity and the abyssal layer could be limited to the base of the superplumes.

1.01.4.4 Stability of the Planetary-Scale Heterogeneities

Richards and Engebretson (1992) mapped four geophysical functions (their Figure 1): geoid, hot-spot locations, velocity anomalies near the CMB, and a sum of the mass of all slabs subducted during the last 120 Ma. Correlation is significant only for degrees 2 and 3. Of the four functions, the first three are surface observables; only the seismic velocity anomalies correspond to a particular depth – the lowermost mantle. Even though Ricard et al. (1993) and Lithgow-Bertelloni and Richards (1998) proposed a model with the sinking slabs distributed at different depths according to their age, correlation between the velocity and the density anomalies (sinking slabs) is poor in the lowermost mantle. This may be called the 'slab sinking paradox': how the velocity anomalies near the CMB may "know" about slabs that are still suspended higher in the mantle? Dziewonski et al. (2010) proposed that this paradox could be explained if the long-term (~100 Ma) slab subduction cyclically repeats itself and the anomalies in the lowermost mantle reflect a long-term average of these cycles. The important degrees are 2 and 3; for each of these degrees, the correlation is very high, but the relative power of degree 2 of seismic anomalies is three times greater than that of degree 3; in integrated slab expansion, degree 3 has higher power than degree 2. This may mean that degree 2 may be more stable in time than degree 3. Because of its apparent longevity, Dziewonski et al. (2010) named the degrees 2 and 3 the 'mantle anchor structure' (MAS).

The degree-2 anomaly, which dominates the abyssal layer, has geometric properties that have led Dziewonski et al. (2010) to a speculation – which some thought 'outrageous' – that degree-2 anomalies may be stable over very long times. What is special about degree-2 is that when translated into density anomalies, it may affect the Earth's nonhydrostatic moment of inertia tensor. **Figure 25** shows a comparison of the degree-2 anomaly at 2800 km depth in 3-D models S362ANI (Kustowski et al., 2008), SAW24B16 (Mégnin and Romanowicz, 2000) and S20RTS (Ritsema et al., 1999). It shows nearly identical images that are very close to the harmonic Y_{20} rotated so that its symmetry axis lies in the equatorial plane. The random test shows that to obtain such a result by chance is less than 1 in 1000. If the negative velocity anomalies are associated with higher effective density, then the minimum moment of inertia axis would be crossing the equator at the center of the red anomalies (about 10° east or 170° west) as required by the rotation dynamics. The solution is degenerate for the other two principal components: any axis

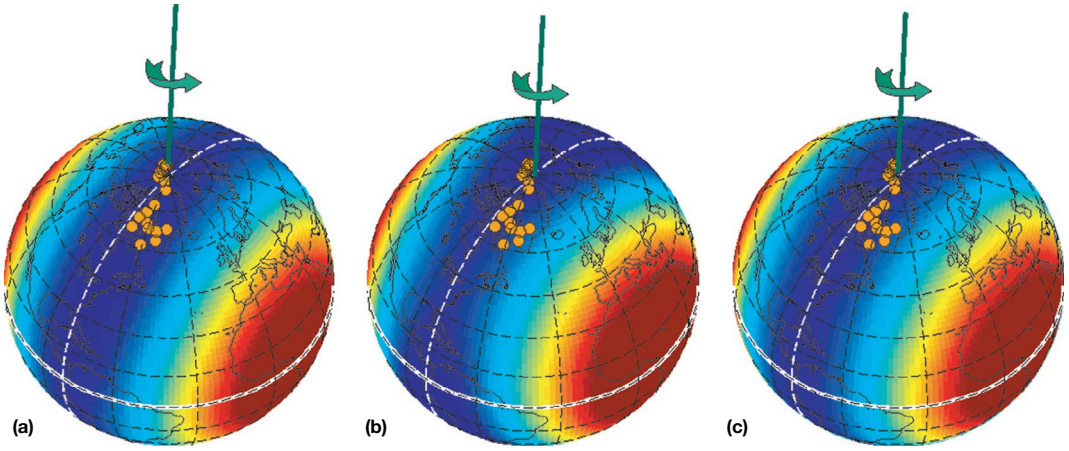

Figure 25 The nearly indistinguishable degree-2 structures at 2800 km depth of three global tomographic S-velocity models: (a) S362ANI (Kustowski et al., 2008), (b) SAW24B16 (Mégnin and Romanowicz, 2000), (c) S20RTS (Ritsema et al., 1999). Pink circles indicate paleopole locations from the true polar wander reconstructions of Besse and Courtillot (2002). Reproduced from Dziewonski A, Lekic, and Romanowicz A (2010) Mantle anchor structure; an argument for bottom up tectonics. *Earth and Planetary Science Letters* 299: 69–79.

passing through the polar great circle crossing the equator at 100° east or 80° west will have the maximum moment of inertia. Thus, this great circle would be the preferred direction of 'true polar wonder' (TPW) due to mass redistribution. The orange dots in Figure 25 are the TPW positions during the last 200 Ma as determined by Besse and Courtillot (2002); the agreement is good even though no TWP observations were included in building the seismic models. Modeling of TPW using geodynamic data was initiated by Steinberger and O-'Connell (1997) and continues till the present (c.f. Conrad et al., 2013; Rouby et al., 2010; Steinberger and Torsvik, 2010). The TPW is increasingly difficult to determine for times before the magnetic stripes on the oceanic floor have been destroyed. Some paleomagnetic evidence exists that the MAS hypothesis is consistent with the data as old as 1.3 Ga (Jean Besse, 2013, personal communication). If this is correct, then there is no reason not to test an assumption that it was formed not long after the Earth's accretion.

1.01.4.5 The Need for Consideration of More Complete Modeling of Mantle Flow

A quadrupole convection essentially identical to the pattern in Figure 25 has been proposed by Busse (1983) and its stability implications pointed out by Le Pichon and Huchon (1984) on the basis of correlation of the degree-2 geoid with velocity anomalies in the lowermost mantle (Dziewonski et al., 1977). With the incomparably higher quality of current global models of heterogeneity, we do not have a mantle flow model that reproduces large-scale features revealed by mantle tomography.

The concepts of 'top-down' or 'bottom-up' tectonics are not contradictory, but rather complementary. The heterosphere of Figure 23 is highly energetic – it contains above 80% of the volume integrated power of mantle heterogeneity – and acts on a relatively short timescale: the pattern of subductions has changed considerably during the last 200 Ma (Lithgow-Bertelloni and Richards, 1998, Figure 6). The lower-mantle heterogeneity structure (superplume zone) shows great stability, as indicated by the 'slab paradox' and TPW results, and may impose the long time influence on the heterosphere's behavior. The 'ETZ' is the critical region in which the communication between the heterosphere and the superplume zone is taking place. It is clear that some slabs become stagnant above the 650 km discontinuity, but the degree-2 velocity anomaly is well correlated with the integrated slabs during the last 15–20 Ma and does not show evidence of earlier accumulation. Thus, it is not clear what happens with the material subducted earlier. It is also not clear how the superplumes interact with the transition zone. The Pacific is slow both below and above the 650 km discontinuity, but this is not as obvious for the African superplume. Romanowicz and Gung (2002) argued that attenuation in the transition zone better reflects its thermal state than the velocity anomalies and that the Q anomalies in the transition zone are well correlated with the velocity anomalies at the CMB.

The paradigm of three-layer mantle dynamics, each of which acts on a different spatial and temporal scale and has been derived mostly from seismic data providing a present-day snapshot of 3-D velocity anomalies, must be tested by geodynamic modeling. From the published results of numerical modeling of mantle flow, it is clear that such a structure with three boundary layers has yet to be realized and match the observations.

With the recent advances in numerical modeling, a clearer picture of the connection between lower-mantle and transition zone structure on the one hand and structure in the asthenosphere on the other hand is starting to emerge. Figure 26 shows a 3-D rendering of the central Pacific portion of upper-mantle model SEMum2 (French et al., 2013), viewed from the east to the west, which shows a number of vertically elongated low-velocity columns (plumes?), many of them rooted in the lower mantle and extending up to about 350 km depth. At shallower depths, this structure is replaced by a series of horizontally elongated low-velocity channels or 'fingers,' aligned parallel to the absolute plate motion and extending into the low-velocity zone right below the lithosphere. These low-velocity channels, which are present in all major ocean basins, are spaced regularly with a wavelength of about 1800–2000 km and manifest the dynamic interaction in the 'heterosphere' between the upwellings from the 'superplume zone' and ETZ (e.g., Figure 23) and the tectonic plates.

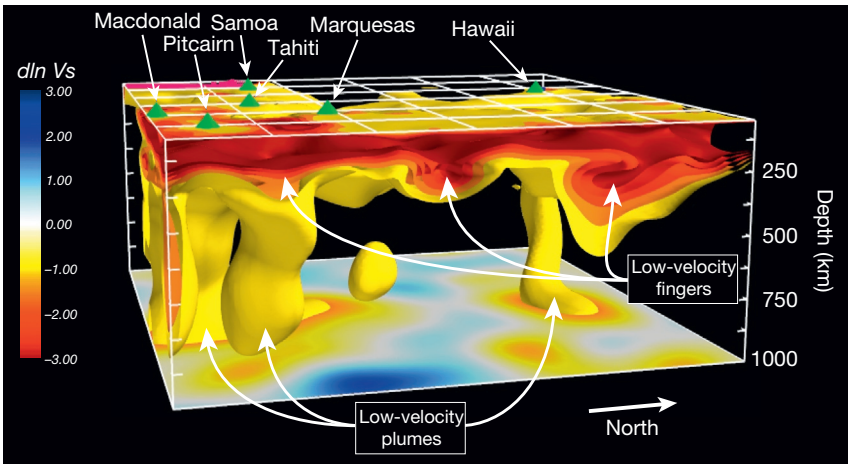

Figure 26 3-D rendering of the low-velocity parts of a portion of model SEMum2 (French et al., 2013) in the central Pacific, shown down to 1000 km depth. The range of velocity anomalies shown is −1% to −3%. The view is from the east, standing in the vicinity of the East Pacific Rise and looking towards the west. Green cones indicate major hot spots. Note the regularly spaced low-velocity fingers right below the very slow low-velocity zone. These fingers extend for several thousand kilometers into the Pacific basin, in the direction of the Pacific Plate absolute plate motion. Similar structures are seen in the south and North Atlantic Ocean and in the Indian Ocean.

We expect that, in the next 5–10 years, these images, as well as those of the lower mantle, will become even sharper, as the frequency range accessible to global tomography based on numerical methods increases, providing definitive clues on such fundamental questions as the relation of hot spots to plumes, and plumes to superplumes, and the role of superplumes in the global mantle circulation and the fate of subducted slabs.

References

Adams RD, et al. (2002) International seismology. In: Lee WHK, Kanamori H, Jennings PC, and Kisslinger C (eds.) *International Handbook of Earthquake and Engineering Seismology Part A*, pp. 29–37. San Diego, CA: Academic Press.

Agnew D, Berger J, Buland R, Farrell W, and Gilbert F (1976) International deployment of accelerometers: A network for very long period seismology. *EOS. Transactions of the American Geophysical Union* 57: 180–188.

Agnew DC, Berger J, Farrell WE, Gilbert JF, Masters G, and Miller D (1986) Project IDA; a decade in review. *EOS. Transactions of the American Geophysical Union* 67: 203–212.

Agnew DC, et al. (2002) History of seismology. In: Lee WHK, Kanamori H, Jennins PC, and Kisslinger C (eds.) *International Handbook of Earthquake and Engineering Seismology*, pp. 3–12. San Diego, CA: Academic Press.

Aki K, Christofferson A, and Husebye E (1977) Determination of the three-dimensional structure of the lithosphere. *Journal of Geophysical Research* 82: 277–296.

Alsop LE, Sutton GH, and Ewing M (1961) Free oscillations of the Earth observed on strain and pendulum seismographs. *Journal of Geophysical Research* 66: 631–641.

Alterman Z, Jarosch H, and Pekeris CL (1959) Oscillations of the Earth. *Proceedings of the Royal Society of London, Series A* 259: 80–95.

Anderson DL (1963) Recent evidence concerning the structure and composition of the Earth's mantle. *Physics and Chemistry of the Earth* 6: 1–129.

Anderson DL and Archambeau CB (1964) The anelasticity of the Earth. *Journal of Geophysical Research* 69: 2071–2084.

Anderson DL and Hart RS (1978) Q of the Earth. *Journal of Geophysical Research* 83: 5869–5882.

Backus GE and Gilbert F (1961) The rotational splitting of free oscillations of the Earth. *Proceedings of the National Academy of Sciences of the United States of America* 47: 362–371.

Backus GE and Gilbert F (1967) Numerical applications of formalism for geophysical inverse problems. *Geophysical Journal of the Royal Astronomical Society* 13: 247–276.

Backus GE and Gilbert F (1968) The resolving power of gross Earth data. *Geophysical Journal of the Royal Astronomical Society* 16: 169–205.

Backus GE and Gilbert F (1970) Uniqueness in the inversion of gross Earth data. *Philosophical Transactions of the Royal Society of London, Series A* 266: 169–205.

Benioff H (1958) Long waves observed in the Kamchatka earthquake of November 2, 1952. *Journal of Geophysical Research* 63: 589–593.

Benndorf H (1905) Über die Art der Fortpflanzung der Erdbebenwellen im Erdinneren. 1. Mitteilung. Sitzungsberichte der Kaiserlichen Akademie in Wien. Mathematisch-Naturwissenschaftliche Klasse 114, Mitteilungen der Erdbebenkommission. *Neue Folge* 29: 1–42.

Benndorf H (1906) Über die Art der Fortpflanzung der Erdbebenwellen im Erdinneren. 2. Mitteilung. Sitzungsberichte der Kaiserlichen Akademie in Wien. Mathematisch-Naturwissenschaftliche Klasse 115, Mitteilungen der Erdbebenkommission. *Neue Folge* 31: 1–24.

Berkner LV and Members of the panel (1959) *Report of the Panel on Seismic Improvement. The Need for Fundamental Research in Seismology*, p. 212. Washington, DC: Department of State.

Besse J and Courtillot V (2002) Apparent and true polar wander and the geometry of the geomagnetic field over the last 200 Myr. *Journal of Geophysical Research* 107: 2300. http://dx.doi.org/10.1029/2000JB000050.

Birch AF (1952) Elasticity and constitution of the Earth's interior. *Journal of Geophysical Research* 57: 227–286.

Boschi L and Dziewonski AM (1999) High' and 'low' resolution images of the Earth's mantle – Implications of different approaches to tomographic modeling. *Journal of Geophysical Research* 104: 25567–25594.

Brune J and Dorman J (1963) *Seismic Waves and the Structure of the Crust and Mantle in the Canadian Shield*: Geological Society of America, pp. 28–29, Special Paper.

Buland R, Berger J, and Gilbert F (1979) Observations from the IDA network of attenuation and splitting during a recent earthquake. *Nature* 277: 358–362.

Bullen KE (1940) The problem of the Earth's density variation. *Bulletin of the Seismological Society of America* 30: 235–250.

Bullen KE (1949) Compressibility-pressure hypothesis and the Earth's interior. *Geophysical Journal of the Royal Astronomical Society* 5: 355–368.

Busse F (1983) Quadrupole convection in the lower mantle. *Geophysical Research Letters* 10: 285–288.

Capdeville Y, Chaljub E, Vilotte JP, and Montagner JP (2003) Coupling the spectral element method with a modal solution for elastic wave propagation in global earth models. *Geophysical Journal International* 152: 34–67. http://dx.doi.org/10.1046/j.1365-246X.2003.01808.x.

Chen P, Jordan TH, and Zhao L (2007) Full three-dimensional tomography: A comparison between the scattering-integral and adjoint-wavefield methods. *Geophysical Journal International* 170: 175–181.

Colli L, Fichtner A, and Bunge H-P (2013) Full waveform tomography of the upper mantle in the south Atlantic region: Imaging a westward fluxing shallow asthenosphere? *Tectonophysics* 604: 26–40.

Conrad CP, Steinberger B, and Torsvik TH (2013) Stability of active mantle upwelling revealed by net characteristics of plate tectonics. *Nature* 498: 479–482.

Cooley JW and Tukey JW (1965) An algorithm for machine computation of complex Fourier series. *Mathematics of Computation* 19: 297–301.

Dahlen F, Hung S-H, and Nolet G (2000) Fréchet kernels for finite-frequency traveltimes – I. Theory. *Geophysical Journal International* 141: 157–174.

Dalton CA (2007) *The global attenuation structure of the upper mantle*. Ph.D. thesis. Harvard University.

Dziewonski AM (1984) Mapping the lower mantle: Determination of lateral heterogeneity in *P*-velocity up to degree and order 6. *Journal of Geophysical Research* 89: 5929–5952.

Dziewonski AM and Anderson DL (1981) Preliminary Earth model (PREM). *Physics of the Earth and Planetary Interiors* 25: 297–356.

Dziewonski AM, Chou T-A, and Woodhouse JH (1981) Determination of earthquake source parameters from waveform data for studies of global and regional seismicity. *Journal of Geophysical Research* 86: 2825–2852.

Dziewonski AM and Gilbert F (1972) Observations of normal modes from 84 recordings of the Alaskan earthquake of 28 March 1964. *Geophysical Journal of Royal Astronomical Society* 27: 393–446.

Dziewonski AM and Gilbert F (1973) Observations of normal modes from 84 recordings of the Alaskan earthquake of 28 March 1964, Part II: Spheroidal overtones from 285–100 seconds. *Geophysical Journal of the Royal Astronomical Society* 35: 401–437.

Dziewonski AM and Gilbert F (1974) Temporal variation of the seismic moment tensor and the evidence of precursive compression for two deep earthquakes. *Nature* 247: 185–188.

Dziewonski AM and Haddon RAW (1974) The radius of the core–mantle boundary inferred from travel time and free oscillation data: A critical review. *Physics of the Earth and Planetary Interiors* 9: 28–35.

Dziewonski AM, Hager BH, and O'Connell RJ (1977) Large scale heterogeneities in the lower mantle. *Journal of Geophysical Research* 82: 239–255.

Dziewonski AM and Hales AL (1972) Numerical analysis of dispersed seismic waves. In: Adler B, Fernbach S, and Bolt BA (eds.) *Methods in Computational Physics*, vol. 11, pp. 39–85. New York: Academic Press.

Dziewonski AM, Hales AL, and Lapwood ER (1975) Parametrically simple Earth models consistent with geophysical data. *Physics of the Earth and Planetary Interiors* 10: 12–48.

Dziewonski AM, Lekic V, and Romanowicz B (2010) Mantle anchor structure: An argument for bottom up tectonics. *Earth and Planetary Science Letters* 299(2010): 69–79.

Dziewonski AM, Lekic V, and Romanowicz B (2013) Planet within a planet: Implications of principal component analysis of global tomographic models. *EOS. Transactions of the American Geophysical Union* 94(Fall Meeting Supplement), Abstract DI32-01.

Dziewonski AM and Steim JM (1982) Dispersion and attenuation of mantle waves through waveform inversion. *Geophysical Journal of the Royal Astronomical Society* 70: 503–527.

Dziewonski A, Su W-J, and Woodward R (1991) Global structures of the Earth's interior. *EOS, Transactions American Geophysical Union, fall meeting:* 72: 451.

Ekström G, Dziewonski AM, Maternovskaya NN, and Nettles M (2005) Global seismicity of 2003: Centroid-moment-tensor solutions for 1087 earthquakes. *Physics of the Earth and Planetary Interiors* 148: 327–351.

Ekström G and Dziewoski AM (1998) The unique anisotropy of the Pacific upper mantle. *Nature* 394: 168–172.

Ekström G, Tromp J, and Larson EW (1997) Measurements and models of global surface wave propagation. *Journal of Geophysical Research* 102: 8137–8157.

Ewing M, Jardetzky WS, and Press F (1957) *Elastic Waves in Layered Media*. New York: McGraw-Hill.

Ewing M and Press F (1954) An investigation of mantle Rayleigh waves. *Bulletin of the Seismological Society of America* 44: 127–148.

Fichtner A, Kennett B, Igel H, and Bunge H (2009) Full seismic waveform tomography for upper mantle structure in the Australasian region using adjoint methods. *Geophysical Journal International* 179: 1703–1725.

French S, Lekic V, and Romanowicz B (2013) Waveform tomography reveals channeled flow at the base of the oceanic asthenosphere. *Science* 342: 227–230.

Fuchs K and Müller G (1971) Computation of synthetic seismograms and comparison with observations. *Geophysical Journal of the Royal Astronomical Society* 23: 417–433.

Fukao Y and Obayashi M (2013) Subducted stagnant slabs above, penetrating through and trapped below the 660 km discontinuity. *Journal of Geophysical Research* 118: 1–19.

Fukao Y, Obayashi M, Inoue H, and Nenbai M (1992) Subducting slabs stagnant in the mantle transition zone. *Journal of Geophysical Research* 97: 4809–4822.

Fukao Y, Obayashi M, and Nakakuki T (2009) the Deep Slab Project Group. *Annual Review of Earth and Planetary Sciences* 37: 19–46. http://dx.doi.org/10.1146/annurev.earth.36.031207.124224.

Fukao Y, Widiyantoro S, and Obayashi M (2001) Stagnant slabs in the upper and lower mantle transition region. *Reviews of Geophysics* 39: 291–323.

Galitzin BB (1914) Vorlesungen über Seismometrie, deutsche Bearbeitung unter Mitwirkung von Clara Reinfeldt (also Golicyn). *Herausgegeben von Oskar Hecker*, vol. VIII, p. 538. Berlin: Verlag Teubner.

Geiger L (1910) Herdbestimmung bei Erdbeben aus den Ankunftszeiten. Nachrichten von der Königlichen Gesellschaft der Wissenschaften zu Göttingen. *Mathematisch-physikalische Klasse*. pp. 331–349 (Translated into English by Peebles FWL, Anthony H, Corey SJ).

Geiger L (1912) Probability method for the determination of earthquake epicenters from the arrival time only. *Bulletin of St. Louis University* 8: 60–71.

Gilbert F and Dziewonski AM (1975) An application of normal mode theory to the retrieval of structural parameters and source mechanisms from seismic spectra. *Philosophical Transactions of the Royal Society of London, Series A* 278: 187–269.

Green RWE and Hales AL (1968) Travel times of P waves to 30 degrees in central United States and upper mantle structure. *Bulletin of the Seismological Society of America* 58: 267–289.

Gu YJ, Dziewonski AM, and Ekström G (2003) Simultaneous inversion for mantle shear velocity and topography of transition zone discontinuities. *Geophysical Journal International* 154: 559–583.

Gu JY, Dziewonski AM, Su W-J, and Ekström G (2001) Shear velocity model of the mantle and discontinuities in the pattern of lateral heterogeneities. *Journal of Geophysical Research* 106: 11169–11199.

Gung Y, Panning M, and Romanowicz B (2003) Global anisotropy and the thickness of continents. *Nature* 422: 707–711.

Gung Y and Romanowicz B (2004) Q tomography of the upper mantle using three component long period waveforms. *Geophysical Journal International* 157: 813–830.

Gutenberg B (1913) Über die Konstitution des Erdinnern, erschlossen aus Erdbebenbeobachtungen. *Physikalische Zeitschrift* 14: 1217–1218.

Hales AL, Lapwood ER, and Dziewonski AM (1974) Parameterization of a spherically symmetrical Earth model with special references to the upper mantle. *Physics of the Earth and Planetary Interiors* 9: 9–12.

Hammer PTC, Clowes RM, Cook FA, van der Velden AJ, and Vosudevan K (2010) The Lithoprobe trans-continental lithospheric cross-sections imaging the internal structure of the North American continent. *Canadian Journal of Earth Sciences* 47: 821–857.

Harjes H-P and Seidl D (1978) Digital recording and analysis of broad-band seismic data at the Gräfenberg (GRF) array. *Journal of Geophysics* 44: 511–523.

Harmon N, Forsyth D, and Weeraratne DS (2009) Thickening of young Pacific lithosphere from high-resolution Rayleigh wave tomography: A test of the conductive cooling model. *Earth and Planetary Science Letters* 278: 96–106.

Haskell NA (1953) The dispersion of surface waves on multilayered media. *Bulletin of the Seismological Society of America* 43: 17–43.

Herglotz G (1907) Über das Benndorfsche Problem der Fortpflanzungsgeschwindigkeit der Erdbebenwellen. *Physikalische Zeitschrift* 8: 145–147.

Houser C, Masters G, Shearer P, and Laske G (2008) Shear and compressional velocity models of the mantle from cluster analysis of long-period waveforms. *Geophysical Journal International* 174: 195–212. http://dx.doi.org/10.1111/j.1365-246X.2008.03763.x.

Jeffreys H (1926) The rigidity of the Earth's central core. *Monthly Notices of the Royal Astronomical Society* 1(Geophysical Supplement): 371–383.

Jeffreys H (1939) The times of P, S and SKS, and the velocities of P and S, month not. *Royal Astronomical Society, Geophysical Supplement* 4: 498–533.

Jeffreys H and Bullen KE (1940) *Seismological Tables*, p. 50. London: British Association for the Advancement of Science.

Jobert N (1956) Évaluation de la période d'oscillation d'une sphere hétérogène, par application du principe de Rayleigh. *Comptes Rendus De L Academie Des Sciences, Paris* 243: 1230–1232.

Jobert N (1957) Sur la période propre des oscillations sphèroïdales de la Terre. *Comptes Rendus De L Academie Des Sciences, Paris* 244: 242–258.

Johnson LR (1967) Array measurements of P velocity in the upper mantle. *Journal of Geophysical Research* 72: 6309–6325.

Jordan TH (1978) A procedure for estimating lateral variations from low-frequency eigenspectra data. *Geophysical Journal of the Royal Astronomical Society* 52: 441–455.

Jordan TH and Anderson DL (1974) Earth structure from free oscillations and travel times. *Geophysical Journal of the Royal Astronomical Society* 36: 411–459.

Julian BR and Sengupta MK (1973) Seismic travel time evidence for lateral inhomogeneity in the deep mantle. *Nature* 242: 443–447.

Kennett BLN, Engdahl ER, and Buland R (1995) Constraints on seismic velocities in the Earth from traveltimes. *Geophysical Journal International* 122: 108–124.
Knott CG (1899) Reflection and refraction of elastic waves, with seismological applications. *The London, Edinburgh, and Dublin Philosophical Magazine and Journal of Science, Series 5* 48, 64–97, 567–569.
Komatitsch D and Tromp J (2002) Spectral-element simulations of global seismic wave propagation: I. Validation. *Geophysical Journal International* 149: 390–412.
Komatitsch D and Vilotte J-P (1998) The spectral element method: An efficient tool to simulate the seismic response of 2D and 3D geological structures. *Bulletin of the Seismological Society of America* 88: 368–392.
Kustowski B, Ekström G, and Dziewonski AM (2008) The shear-wave velocity structure in the upper mantle beneath Eurasia. *Geophysical Journal International* 174: 978–992.
Landisman M, Sato Y, and Nafe JE (1965) Free vibrations of the Earth and the properties of its deep interior regions: Part 1. Density. *Geophysical Journal of the Royal Astronomical Society* 9: 439–502.
Le Pichon X and Huchon P (1984) Geoid, Pangea and convection. *Earth and Planetary Science Letters* 67: 123–135.
Lehmann I (1936) P'. *Publ. Bureau Cent. Séism. Inter., Série A, Trav. Scient* 14: 87–115.
Lekic V, Cottaar S, Dziewonski AM, and Romanowicz B (2012) Cluster analysis of global lower mantle tomography: A new class of structure and implications for chemical heterogeneity. *Earth and Planetary Science Letters* 357–358: 68–77.
Lekic V and Romanowicz B (2011) Inferring upper-mantle structure by full waveform tomography with the spectral element method. *Geophysical Journal International* 185: 799–831.
Li XD and Romanowicz B (1995) Comparison of global waveform inversions with and without considering cross branch coupling. *Geophysical Journal International* 121: 695–709.
Li X-D and Romanowicz B (1996) Global mantle shear velocity model developed using nonlinear asymptotic coupling theory. *Journal of Geophysical Research* 101: 22245–22272.
Li XD and Tanimoto T (1993) Waveforms of long-period body waves in a slightly aspherical Earth model. *Geophysical Journal International* 112: 92–102.
Lithgow-Bertelloni C and Richards MA (1998) The dynamics of Cenozoic and Mesozoic plate motions. *Reviews of Geophysics* 36: 27–78.
Liu H-P, Anderson DL, and Kanamori H (1976) Velocity dispersion due to anelasticity: Implications for seismology and mantle composition. *Geophysical Journal of the Royal Astronomical Society* 47: 41–58.
Lognonné P (1991) Normal modes and seismograms in an anelastic rotating Earth. *Journal of Geophysical Research* 96: 20309–20319.
Lognonné P and Romanowicz B (1990) Modelling of coupled normal modes of the Earth: The spectral method. *Geophysical Journal International* 102(2): 365–395.
Love AEH (1911) *Some Problems of Geodynamics*. Cambridge: Cambridge University Press.
Masters G, Jordan TH, Silver PG, and Gilbert F (1982) Aspherical earth structure from fundamental spheroidal mode data. *Nature* 298: 609–613.
Mégnin C, Bunge HP, Romanowicz B, and Richards MA (1997) Imaging 3-D spherical convection models: What can seismic tomography tell us about mantle dynamics? *Geophysical Research Letters* 24(11): 1299–1302.
Mégnin C and Romanowicz B (1999) The effects of the theoretical formalism and data selection on mantle models derived from waveform tomography. *Geophysical Journal International* 138: 366–380.
Mégnin C and Romanowicz B (2000) The three-dimensional shear velocity structure of the mantle from the inversion of body, surface and higher-mode waveforms. *Geophysical Journal International* 143(3): 709–728.
Mendiguren J (1973) Identification of free oscillation spectral peaks for 1970 July 31, Colombian deep shock using the excitation criterion. *Geophysical Journal of the Royal Astronomical Society* 33: 281–321.
Mohorovičić A (1910) Potres od 8. X 1909. God. Izvjesće Zagr. met. Ops. Zag. 1909, Zagreb (Das Beben vom 8. X 1909. Jahrbuch des meteorologischen Observatoriums in Zagreb f ür das Jahr 1909), 9, Part 4, 1–63.
Montelli R, Nolet G, Dahlen F, Masters G, Engdahl E, and Hung SH (2004a) Global P and PP travel time tomography: Rays vs. waves. *Geophysical Journal International* 158: 637–654.
Montelli R, Nolet G, Dahlen F, Masters G, Engdahl E, and Hung SH (2004b) Finite-frequency tomography reveals a variety of plumes in the mantle. *Science* 303: 338–343.
Ness NF, Harrison JC, and Slichter LB (1961) Observations of the free oscillations of the Earth. *Journal of Geophysical Research* 66: 621–629.
Nolet G and Dahlen FA (2000) Wave front healing and the evolution of seismic delay times. *Journal of Geophysical Research* 105: 19043–19054.
Oldham RD (1906) The constitution of the interior of the Earth, as revealed by earthquakes. *Quarterly Journal of the Geological Society* 62(1–4): 456–475.
Panning M and Romanowicz B (2006) A three dimensional radially anisotropic model of shear velocity in the whole mantle. *Geophysical Journal International* 167: 361–379.
Park J, Butler R, Anderson K, et al. (2005) Performance review of the global seismographic network for the Sumatra–Andaman megathrust earthquake. *Seismological Research Letters* 76(3): 331–343.
Pekeris CL, Alterman Z, and Jarosch H (1961a) Comparison of theoretical with observed values of the periods of the free oscillations of the Earth. *Proceedings of the National Academy of Sciences of the United States of America* 47: 91–98.
Pekeris CL, Alterman Z, and Jarosh H (1961b) Rotational multiplets in the spectrum of the Earth. *Physical Review* 122: 1692–1700.
Pekeris CL and Jarosch H (1958) The free oscillations of the Earth. In: Benioff H, Ewing M, HowellJun BF, and Press K (eds.) *Contributions in Geophysics in Honor of Beno Gutenberg*, pp. 171–192. New York: Pergamon.
Peter D, Tape C, Boschi L, and Woodhouse JH (2007) Surface wave tomography: Global membrane waves and adjoint methods. *Geophysical Journal International* 171: 1098–1117. http://dx.doi.org/10.1111/j.1365-246X.2007.03554.x.
Peterson J, Butler HM, Holcomb LT, and Hutt C (1976) The seismic research observatory. *Bulletin of the Seismological Society of America* 66: 2049–2068.
Poupinet G, Frechet J, and Thouvenot F (1989) Portable short period vertical seismic stations transmitting via telephone or satellite. In: Cassinis R and Nolet G (eds.) *Digital Seismology and Fine Modelling of the Lithosphere*, pp. 9–26. London: Plenum.
Press F (1956) Determination of crustal structure from phase velocity of Rayleigh waves – Part I. Southern California. *Bulletin of Geological Society of America* 67: 1647–1658.
Ricard Y, Richards M, Lithgow-Bertelloni C, and LeStunff YL (1993) A geodynamic model of mantle density heterogeneity. *Journal of Geophysical Research* 98: 21895–21910.
Richards M and Engebretson D (1992) Large-scale mantle convection and the history of subduction. *Nature* 355: 437–440.
Rickers F, Fichtner A, and Trampert J (2013) The Iceland–Jan Mayen plume system and its impact on mantle dynamics in the North Atlantic region: Evidence from full-waveform inversion. *Earth and Planetary Science Letters* 367: 39–51.
Ritsema J, Deuss A, van Heijst HJ, and Woodhouse J (2011) HS40RTS: A degree-40 shear-velocity model for the mantle from new Rayleigh wave dispersion, teleseismic traveltime and normal-mode splitting function measurements. *Geophysical Journal International* 184: 1223–1236.
Ritsema J, van Heijst HH, and Woodhouse JH (1999) Complex shear wave velocity structure imaged beneath Africa and Iceland. *Science* 286: 1925–1928.
Ritsema J, van Heijst HJ, and Woodhouse JH (2004) Global transition zone tomography. *Journal of Geophysical Research* 109. B02302: http://dx.doi.org/10.1029/2003JB002610.
Romanowicz B (1979) Seismic structure of the upper mantle beneath the United States by three-dimensional inversion of body wave arrival times. *Geophysical Journal of the Royal Astronomical Society* 57: 479–506.
Romanowicz B (1991) Seismic tomography of the Earth's mantle. *Annual Review of Earth and Planetary Science* 19: 77–99.
Romanowicz B (2003) Global mantle tomography: Progress status in the last 10 years. *Annual Review of Geophysics and Space Physics* 31: 303–328.
Romanowicz BA, Cara M, Fels JF, and Rouland D (1984) Geoscope: A French initiative in long-period three-component seismic networks. *EOS. Transactions of the American Geophysical Union* 65: 753–754.
Romanowicz BA and Dziewonski AM (1986) Towards a federation of broadband seismic networks. *EOS. Transactions of the American Geophysical Union* 67: 541–542.
Romanowicz B and Gung Y (2002) Superplumes from the core–mantle boundary to the lithosphere: Implications for heat flux. *Science* 296(2002): 513–516.
Romanowicz B, Karczewski J-F, et al. (1991) The GEOSCOPE program: Present status and perspectives. *Bulletin of the Seismological Society of America* 81: 243–264.
Rouby H, Greff-Lefftz M, and Besse J (2010) Mantle dynamics, geoid, inertia and TPW since 120 Myr. *Earth and Planetary Science Letters* 292: 301–311.
Roult G, Montagner JP, Romanowicz B, et al. (2010a) The GEOSCOPE program: Progress, and challenges during the past 30 years. *Seismological Research Letters* 81: 428–452.
Roult G, Montagner J-P, Romanowicz B, et al. (2010b) The GEOSCOPE Program: Progress and challenges during the past 30 years. *Seismological Research Letter* 81: 429–452.
Russakoff D, Ekström G, and Tromp J (1998) A new analysis of the great 1970 Colombia earthquake and its isotropic component. *Journal of Geophysical Research* 102: 20423–20434.
Sailor RV and Dziewonski AM (1978) Observations and interpretation of attenuation of normal modes. *Geophysical Journal of the Royal Astronomical Society* 53: 559–581.

Schweitzer J (2007) In: Gubbins D and Herrero-Bervera E (eds.) *Encyclopedia of Geomagnetism and Paleomagnetism*: Kluwer-Springer, ISBN:1-4020-3992-1 (in print).

Simmons NA, Forte AM, and Grand SP (2009) Joint seismic, geodynamic and mineral physical constraints on three-dimensional mantle heterogeneity: Implications for the relative importance of thermal versus compositional heterogeneity. *Geophysical Journal International* 177: 1284–1304.

Simmons NA, Forte A, Boschi L, and Grand S (2010) GyPSuM: a joint tomographic model of mantle density and seismic wave speeds. *Journal of Geophysical Research* 115(B12310). http://dx.doi.org/10.1029/2010JB007631.

Souriau A and Souriau M (1983) Test of tectonic models by great-circle Rayleigh waves. *Geophysical Journal of the Royal Astronomical Society* 73: 533–551.

Steim JM (1986) *The very-broad-band seismograph*. Doctoral Thesis, Cambridge, MA: Department of Geological Sciences, Harvard University, p. 184.

Stein S and Wysession M (2003) *An Introduction to Seismology, Earthquakes and Earth Structure*. Oxford: Blackwell, ISBN: 0865420785.

Steinberger B and O'Connell RJ (1997) Changes of the Earth's rotation axis owing to advection of mantle density heterogeneities. *Nature* 387: 169–173.

Steinberger B and Torsvik TH (2010) Toward an explanation for the present and past locations of the poles. *Geochemistry, Geophysics, Geosystems*. http://dx.doi.org/10.1029/2009GC002889.

Stoneley R (1928) A Rayleigh wave problem. *Proceedings of the Leeds Philosophical and Literary Society (Science Section)* 1: 217–225.

Su W-J and Dziewonski AM (1991) Predominance of long-wavelength heterogeneity in the mantle. *Nature* 352: 121–126.

Su W-J and Dziewonski AM (1992) On the scale of mantle heterogeneity. *Physics of the Earth and Planetary Interiors* 74: 29–54.

Takeyuchi H (1959) Torsional oscillations of the Earth and some related problems. *Geophysical Journal of the Royal Astronomical Society* 2: 89–100.

Tape C, Liu Q, Maggi A, and Tromp J (2010) Seismic tomography of the southern California crust based on spectral-element and adjoint methods. *Geophysical Journal International* 160: 195–216.

Tarantola A (2005) *Inverse Problem Theory and Methods for Model Parameter Estimation*. Philadelphia, PA: Society for Industrial and Applied Mathematics.

Thomson ST (1950) Transmission of elastic waves through a stratified solid medium. *Journal of Applied Physics* 21: 89–93.

Toksöz MN and Anderson DL (1966) Phase velocities of long-period surface waves and structure of the upper mantle. *Journal of Geophysical Research* 71: 1649–1658.

Torsvik TH, Steinberger B, Cocks LRM, and Burke K (2008) Longitude: Linking Earth's ancient surface to its deep interior. *Earth and Planetary Science Letters* 276: 273–282.

Tromp J, Tape C, and Liu Q (2005) Seismic tomography, adjoint methods, time reversal and banana doughnut kernels. *Geophysical Journal International* 160: 195–216.

Udias A and Stauder W (2002) The Jesuit contribution to seismology. In: Lee WHK, Kanamori H, Jennins PC, and Kisslinger C (eds.) *International Handbook of Earthquake and Engineering Seismology*, pp. 19–27. San Diego, CA: Academic Press.

van der Hilst RD and deHoop MV (2005) Banana-doughnut kernels and mantle tomography. *Geophysical Journal International* 163: 956–961.

van der Hilst R, Kennett B, Christie D, and Grant J (1994) Project Skippy explores the lithosphere and upper mantle below Australia. *EOS. Transactions of the American Geophysical Union* 75(177): 180–181.

van Heijst HJ and Woodhouse JH (1997) Measuring surface-wave overtone phase velocities using a mode-branch stripping technique. *Geophysical Journal International* 131: 209–230.

von Rebeur-Paschwitz E (1889) The earthquake of Tokyo, April 18, 1889. *Nature* 40: 294–295.

von Rebeur-Paschwitz E (1895) Horizontalpendal-Beobachtungen auf der Kaiserlichen Universitats-Sternwarte zu Strassburg 1892–1894. *Gerlands Beiträge zur Geophysik* 2: 211–536.

Wiechert E (1907) Über Erdbebenwellen. Theoretisches über die Ausbreitung der Erdbebenwellen. *Nachrichten von der Königlichen Gesellschaft der Wissenschaften zu Göttingen, Mathematisch-physikalische Klasse*, pp. 413–529.

Wielandt E (2002) Seismic sensors and their calibration. In: Bormann IP (ed.) *IASPEI New Manual of Seismological Observatory Practice*, vol. 1, pp. 1–46. Potsdam: GeoForschungsZentrum Potsdam, Chapter 5.

Wielandt E and Steim JM (1986) A digital very-broad-band seismograph. *Annales Geophysicae* 4: 227–232.

Wielandt E and Streckeisen G (1982) The leaf-spring seismometer: Design and performance. *Bulletin of the Seismological Society of America* 72: 2349–2367.

Woodhouse JH and Dahlen FA (1978) The effect of a general aspherical perturbation on the free oscillations of the Earth. *Geophysical Journal of the Royal Astronomical Society* 53: 335–354.

Woodhouse JH and Dziewonski AM (1984) Mapping the upper mantle: Three dimensional modeling of earth structure by inversion of seismic waveforms. *Journal of Geophysical Research* 89: 5953–5986.

Woodhouse J and Dziewonski A (1986) Three dimensional mantle models based on mantle wave and long period body wave data. *EOS. Transactions of the American Geophysical Union* 67: 307.

Woodhouse JH and Dziewonski AM (1989) Seismic modelling of the Earth's large-scale three dimensional structure. *Philosophical Transactions of the Royal Society of London, Series A* 328: 291–308.

Woodhouse JH and Girnius TP (1982) Surface waves and free oscillations in a regionalized Earth model. *Geophysical Journal International* 68: 653–673.

Woodward RL, Dziewonski AM, and Peltier WR (1994) Comparisons of seismic heterogeneity models and convective flow calculations. *Geophysical Research Letters* 21: 325–328.

Woodward RL and Masters G (1991) Lower-mantle structure from *ScS-S* differential travel times. *Nature* 352: 231–233.

Zhu H, Bozdag E, Peter D, and Tromp J (2012) Structure of the European upper mantle revealed by adjoint tomography. *Nature Geoscience* 5: 493–498.

Zöppritz K (1907) Über Erdbebenwellen. II: Laufzeitkurven. *Nachrichten von der Königlichen Gesellschaft der Wissenschaften zu Göttingen, Mathematisch-physikalische Klasse:* 529–549.

Relevant Website

http://www.globalcmt.org – Global CMT Web Page.